UNIVERSIDADE DE SÃO PAULO
INSTITUTO DE FÍSICA DE SÃO CARLOS

Claudio Alves Pessoa Junior

Matter-wave interferometry for quantum sensing

São Carlos

2024

Claudio Alves Pessoa Junior

Matter-wave interferometry for quantum sensing

Dissertation presented to the Graduate Program in Physics at the Instituto de Física de São Carlos da Universidade de São Paulo, to obtain the degree of Master in Science.

Concentration area: Theoretical and Experimental Physics

Advisor: Prof. Dr. Philippe Wilhelm Courteille

Corrected version
(Original version available on the Program Unit)

São Carlos
2024

I AUTHORIZE THE REPRODUCTION AND DISSEMINATION OF TOTAL OR PARTIAL COPIES OF THIS DOCUMENT, BY CONVENTIONAL OR ELECTRONIC MEDIA FOR STUDY OR RESEARCH PURPOSE, SINCE IT IS REFERENCED.

Pessoa Junior, Claudio Alves
Matter-wave interferometry for quantum sensing / Claudio Alves Pessoa Junior; advisor Philippe Wilhelm Courteille - corrected version -- São Carlos 2024.
67 p.

Dissertation (Master's degree - Graduate Program in Theoretical and Experimental Physics) -- Instituto de Física de São Carlos, Universidade de São Paulo - Brasil , 2024.

1. Quantum sensing. 2. Strontium. 3. Optical ring cavity. 4. Matter interferometry. I. Courteille, Philippe Wilhelm, advisor. II. Title.

I dedicate this work to all the teachers and professors who allowed me to have come this far, for without them, I would have never reached this moment.

ACKNOWLEDGEMENTS

Muita gente pra agradecer durante todo esse meu processo de formação, mas não vou me alongar aqui. Se por algum acaso eu deixei de te mencionar, lembre-se de que eu estava surtando enquanto escrevia.

Primeiramente gostaria de agradecer todo suporte e incentivo que tive da minha família, por todos os momentos que me ajudaram, seja durante meus surtos e reclamações sobre como o dinheiro acabou com a ciência e outras de minhas revoltas ou seja nos momentos de distração falando coisas que não fazem sentido pra ninguém (acho que nem pra gente faz sentido e isso é mais específico para a primaiada da família).

As pessoas aqui do IFSC que se tornando especiais pra mim, espero ter tocado suas vidas assim como vocês tocaram a minha. Esse é o grupo a quem mais devo às discussões com café, fofocas durante o almoço e saídas que nunca vou, exceto quando digo que vou. Muito obrigado Lilo, Guincho, Gustavo, Rogério, Konaka, Henrique, Adonai, Thalyta e Larissa. Também agradecer aos meus amigos de laboratório (e os que já foram pra melhor também) que me auxiliam tanto e sempre com diversão, apesar de tanto desastre esse ano no lab. Obrigado Pablo, Matheus, Ana, Dalila, Márcia, PH e Gustavo. Importante citar a importância do Aloja nessa caminhada, que me permitiu chegar até aqui, além de me fazer conhecer amigos como Rafaela, Soymara e Victor.

Agradecer também aos dois que me acompanharam acadêmmicamente nessa jornada, o Prof. Doutor Philippe W. Courteille e o Prof. Doutor Raul C. Teixeira, por terem paciência (ou não) comigo e a tentarem passar parte de seus conhecimentos pra mim. Espero um dia poder retribuir por isso de alguma forma.

Menções especiais para algumas pessoinhas que tem importância pra mim em algum ramo da minha vida. À minha mamãe por sempre estar comigo sabendo os momentos em que eu preciso de uma bronca e os momentos que eu preciso de um abraço; ao meu irmão que é quem mais escuta minhas reclamações e com quem as conversas podem ser profundas sem parecer uma chatice, à minha avó materna por seu cafézinho maravilhoso e sempre estar comigo conversando; à Sophia, minha namorada e ser mais incrível, com quem desejo dividir a minha vida; ao Gustavo por ter sido tão companheiro, principalmente no ano de 2023; e ao Rogério pelas várias horas de conversa, na frente de um PC tanto resolver um problema de gravitação e pela amizade.

Por fim, os agradecimentos àqueles que me ajudaram nas correções do texto, correção de física e etc, pois só assim eu considerei isto aqui foi possível. Obrigado Sophia, Dalila, Angela Giampedro (Centro Cultural da USP-São Carlos) e principalmente ao meu orientador.

ABSTRACT

PESSOA JUNIOR, C. A. **Matter-wave interferometry for quantum sensing**. 2024. 67p. Dissertation (Master in Science) - Instituto de Física de São Carlos, Universidade de São Paulo, São Carlos, 2024.

This dissertation reports on advancements in the construction of a quantum sensor for gravimetry based on matter interferometry. Ultra-cold strontium atoms (in the order of 1 μK) within a ring cavity in the bad cavity regime constitute the experimental setup and two distinct approaches were adopted for the comprehension of the system's operation. The first involved simulations of Ramsey-Bordé pulse sequence, specifically the $\pi/2$-π-$\pi/2$-spin echo sequence using the 689 nm transition of strontium. The sequence is commonly employed in matter interferometers and the simulations provided insights for future measurements. The expected precision of our system is within $\Delta g/g < 10^{-8}$, showcasing its potential accuracy. The second approach focused on monitoring Bloch oscillations resulting from the interaction between atoms and cavity light, which induces a frequency proportional to the external force, in our case, gravity. Efforts were made during the experiment towards confirming the system's regime, leading to a significant observation of nonlinear Normal-mode splitting due to high saturation in the strong coupling regime, exhibiting a bi-stable behaviour.

Keywords: Quantum sensing. Strontium. Optical ring cavity. Matter interferometry.

RESUMO

PESSOA JUNIOR, C. A. **Interferometria de onda-matéria para sensoriamento quântico**. 2024. 67p. Dissertação (Mestrado em Ciências) - Instituto de Física de São Carlos, Universidade de São Paulo, São Carlos, 2024.

Com o objetivo de se obter um sensor quântico para gravimetria, esse trabalho relata os avanços na construção de tal sensor baseando-se em interferometria de matéria e utilizando átomos de estrôncio ultrafrios (na ordem de 1 μK) em uma cavidade anelar, no regime de *bad cavity.* Para o funcionamento do sistema, o estudamos através de duas diferentes abordagens: a primeira foi realizando simulações para a sequência de pulsos de Ramsey-Bordé, $\pi/2$-π-$\pi/2$-spin echo- como sequência dos pulsos utilizando a transição 689 nm do estrôncio. Esse tipo de sequência é comumente utilizada em interferômetros de matéria, sendo tais simulações para futuras medidas a serem realizadas. Nessa abordagem podemos observar a possível precisão de nosso sistema, sendo esta $\Delta g/g < 10^{-8}$. A segunda abordagem é por meio do monitoramento das oscilações de Bloch que ocorrem através da interação entre os átomos e a luz da cavidade, resultando em uma frequência proporcional a força externa, que em nosso experimento é a gravidade. Durante a execução do experimento, buscou-se confirmar o regime ao qual o sistema se encontra e com isso tivemos um importante resultado, a observação do *Normal-mode splitting* não-linear devido a alta saturação que ocorre no regime de alto acoplamento, apresentando um comportamento bi-estável.

Palavras-chave: Sensoriamento quântico. Estrôncio. Cavidade anelar. Interferometria de matéria.

LIST OF FIGURES

Figure 1 – Spectral lines of ^{88}Sr. Transition wavelength (transition width in terms of $\Gamma/(2\pi)$). 18

Figure 2 – Cavity with identification of mirrors (HR - *high reflection*) and the positions in which light can enter and exit. 19

Figure 3 – Illustration of sensing using an optical cavity. 20

Figure 4 – Main scheme of our experiment. According to the inset, even if the atoms are in the same state, their spins remain uncorrelated. 21

Figure 5 – (left) Single two-level atom Bloch sphere. (right) Collective Bloch sphere for N non-interacting atoms where the total spin is equal to the sum of all spins. Consequently, the Bloch sphere for the spin will be the collective Bloch sphere with a ratio equal to $\frac{1}{2}N$ ratio. 22

Figure 6 – Scattering of matter interacting with one of the two waves generated by the laser reflected by the mirror. 24

Figure 7 – Ramsey-Bordé Interferometer. Red and green arrows represent $\pi/2$ and π pulses, respectively, and the described states show the transfer of momentum after each pulse starting from an initial state $|a, \vec{p}\rangle$. Black arrows indicate the location of such states. The time between the pulses is T', which is necessary for the occurrence of temporal evolution. In general, momentum is given by vector $\vec{p}$; however, only one direction is normally chosen (p_z). 27

Figure 8 – Bloch Sphere. The three pulses used for interferometry, with a $\pi/2-$pulse in red, creating initially a superposition state, and a $\pi-$pulse in green, generate a temporal evolution in the superposition and adding phase. Towards finishing the sequence, a second $\pi/2-$pulse sends the atoms to one of the two states. Interference occurs with atoms that finish in the same level, but with a different path - some of them will be in state $|p_z\rangle$ after the first $\pi/2-$pulse and others will be in $|p_z + 2\hbar k_e\rangle$, *i.e.* in a superposition of both states. 28

Figure 9 – Energy bands in a system with periodic potential. 30

Figure 10 – Complete experimental setup. 33

Figure 11 – Blue System. 34

Figure 12 – Absorption images taken (a) with atoms – consequently, an absorption shadow is present; (b) without atoms - the image contains all information of our imaging beam (including distortions in the profile) - note the scale goes up to 2600, which relates to the pixel depth of our camera (12bits); and (c) optical density resulting from the subtraction of the images. A dark image containing information on the camera noise was also used; however, it is not relevant for the understanding of the principle. 36
Figure 13 – Red System. 37
Figure 14 – Signals of lock methods of Lock-in and PDH. (a) A full scan of the piezo from the ring cavity shows the two spectra for both finesses. Reflection valleys are reallocated for comparisons. (b) and (c) are signals after the circuits of Lock-in and PDH, respectively. 38
Figure 15 – Science chamber System with cavity trap laser and probe laser separated by polarization. 39
Figure 16 – Signal showing the operation of 3D red MOT, with frequency and power ramp necessary for trapping a larger quantity of atoms. (a) frequency oscillation to trap the fastest atoms due to Doppler effect in blue and power ramp in red. (b) magnetic field during the transference of atoms from blue MOT to red MOT. 40
Figure 17 – Apparatus for power balancing, alignment, polarization, and repumpers of blue and red MOTs, resulting in the three arms of MOT. 41
Figure 18 – Bandwidth κ for the two different polarizations, s (green curve) with $\kappa_s \sim 4\ MHz$ and p (red curve) with $\kappa_p \sim 40\ MHz$, also called high and low finesse, respectively. 42
Figure 19 – (left) Laser scheme. (center) Detunings of the involved lasers (right) Scheme of the experiment. 43
Figure 20 – (left) Cavity transmission spectra without atoms, (right) with atoms. Red curve is a fit considering only the region between $(-8, 8)\ MHz$, which is the range of the probe scan. 44
Figure 21 – (left) Classical normal mode splitting, (right) normal mode splitting in presence of a non-linearity near resonance. 45
Figure 22 – (up left) Theoretical calculation of normal mode spectra without saturation effects, (upright) taking into account saturation effects and (down) signal for both cases with $\Delta_a = 0$ compared to Figure 21 and in ${}^1S_0 \rightarrow {}^3P_1$ transition. 47
Figure 23 – (left) Experimental data of normal mode spectra with saturation effects using false colour image. Dashed line represents the numerical calculations provided in Figure 22. (right) Experimental data of one value of Δ_a for NMS, as expected. 48

Figure 24 – Intensity scan of NMS in false colour image. Increase in the power of the probe laser from left to right in both images. The distinction between them arises from the scanning direction, revealing a bi-stable behavior within our system. Moreover, the high saturation in the probe laser prevents observations of the NMS central peak. 49

Figure 25 – Scheme of a Ramsey-Bordé interferometer considering gravity the external force acting only on $z-$axis, with the states presented in Figure 7. 50

Figure 26 – A comparison among three π-pulses revealed higher intensity leads to increased saturation, whereas longer pulse duration results in greater interaction with gravity. The area of the pulse must remain constant. . 50

Figure 27 – Momentum distributions during a Ramsey-Bordé pulse sequence with $N = 10^5$ strontium atoms of temperature $T = 1\ \mu K$ subject to Bragg pulses at $\lambda_{brg} = 689\ nm$ $({}^1S_0 \rightarrow {}^3P_1)$ under 180° angle (a) after the first $\frac{\pi}{2}$-pulse, (b) after π-pulse, and (c) after the second $\frac{\pi}{2}$-pulse. The gravitational acceleration is $g = 9.81\ m/s^2$. Rabi frequency is $\Omega_R = (2\pi)\ 500\ kHz$ and free evolution time $\tau = 100\ \mu s$. 53

Figure 28 – Impact of temperature on Ramsey fringes. (a,b) $T = 0.1\ \mu K$ and (c,d) $T = 1\ \mu K$. Blue and red curves are calculated for $g = 9.81\ m/s^2$ and are below cyan and magenta. Cyan and magenta lines for $g(1+10^{-2})$. The other parameters are the same adopted in Figure 27, except for $\tau = 200\ \mu s$. (b,d) show the same image of (a,c), respectively, but a zoom near $k_z = 0$ enables distinguishing the blue curve from the cyan one, which represents a 10^{-2} difference in gravity. Since red and magenta curves are in a $B(k_z+2q)$velocity distribution, they cannot be visualized in a zoomed image near $k_z = 0$. 54

Figure 29 – Impact of the free evolution time duration on Ramsey fringes. Blue curves are calculated with $g = 9.81\ m/s^2$ and cyan ones are calculated with (a) $g = g(1 + 10^{-2})g$, $\tau = 200\ \mu s$, (b) $g = g(1 + 10^{-4})g$, $\tau = 2\ ms$, (c) $g = g(1 + 10^{-6})g$, $\tau = 20\ ms$. The other parameters are the same adopted in Figure 28. The images are zoomed in Figure 28(b,d) so that the difference between the curves can be visualized. For longer temporal evolution, the velocity distribution must be zoomed for the visualization of the difference in the signals. 55

Figure 30 – Number of atoms that can be attributed to one of the momenta states $|p\rangle$ (blue curve) or $|p + 2q\rangle$ (red curve) as a function of gravity. Here, $T = 1\ \mu K$, $\tau = 10\ ms$, $\Omega_R = (2/\pi)\ 1\ MHz$. 56

CONTENTS

1 INTRODUCTION 17
1.1 Quantum Sensing and Metrology 17
1.2 Why quantum sensing using cavities? 20

2 THEORETICAL FUNDAMENTALS 23
2.1 Matter-Wave Interferometers 23
2.2 Ramsey-Bordé Interferometer 26
2.3 Bloch Oscillations 29

3 EXPERIMENT 33
3.1 Blue System 34
3.2 Red System 35
3.3 Science Chamber 39
3.3.1 3D Blue and Red MOT 40
3.3.2 Ring Cavity 41
3.4 High-coupling regime and normal-mode splitting 42
3.5 Ramsey-Bordé Pulses Implementation 44

4 RESULTS 47
4.1 Non-linear normal-mode splitting 47
4.2 Numerical simulation of the sensitivity of Ramsey-Bordé pulse sequences 48
4.2.1 Phase shift in a Ramsey-Bordé interferometer 49
4.2.1.1 Bragg diffraction in a Ramsey-Bordé interferometer 51
4.2.2 Measured signals 55

5 CONCLUSIONS 57

REFERENCES 59

APPENDIX 65

APPENDIX A – SCHRÖDINGER EQUATION SOLUTION 67

1 INTRODUCTION

For several decades, aspirations for dominance in science, technology, economy, and other areas have spurred governments - including the Brazilian one (1–7) - to heavily and continuously invest in advancements in quantum information technologies (8–12).

Quantum information technology rests on three pillars, namely, quantum processing, quantum communication, and quantum sensing. Brazil has made efforts to being present in all of them, *i.e.*, in processing (13–16), communication (17–19), and sensing (20). The research project presented in this dissertation belongs to the latter area.

1.1 Quantum Sensing and Metrology

Metrology is a field of science dedicated to measuring quantities in Physics. From basic tasks, like counting livestock, to measuring interplanetary distances, improvements in the precision of tools for measurements have not only accompanied the evolution of science and human knowledge, but also been frequently essential enablers.

Quantum sensing has played an increasingly important role in the quest for measurements of quantities with ever higher precision. The idea is to exploit some particularities of quantum systems, such as ability to form quantum superpositions or even quantum entanglement, which can be very sensitive to environmental conditions and thus react very sensitively to external forces. Quantum sensors are currently used in many fields of fundamental physics, including cosmology in the search for dark matter (21–26).

An example of an external force interesting to be measured is gravity. Since its description by Sir Isaac Newton, its measurement has greatly evolved. In the simplest case, gravimeters measure gravitational acceleration g via trajectory of a massive falling body. However, acceleration is not homogeneous - not only does it depend on the distance of the test mass from the centre of the Earth, but inhomogeneous mass distribution within the Earth's crust causes local variations in gravity, such that $g = g(\mathbf{r})$ must be considered a field (27–29). Modern gravimeters are able to detect deformations of the gravitational field caused *e.g.* by underground caves, aquifers, or other resources.

All gravimeters must employ heavy masses for measuring their gravitational acceleration. The heaviest quantum particles that can be controlled with powerful state-of-the-art technologies, such as cooling or trapping, are atoms. Ultracold clouds of atoms can be prepared in coherent superpositions of different trajectories in arrangements called matter wave interferometers. Two different interferometric techniques already tested are pulsed Ramsey-Bordé interferometer (30–32) and Bloch oscillation (33, 34), both presented in this dissertation. The atomic species chosen is strontium ^{88}Sr (20).

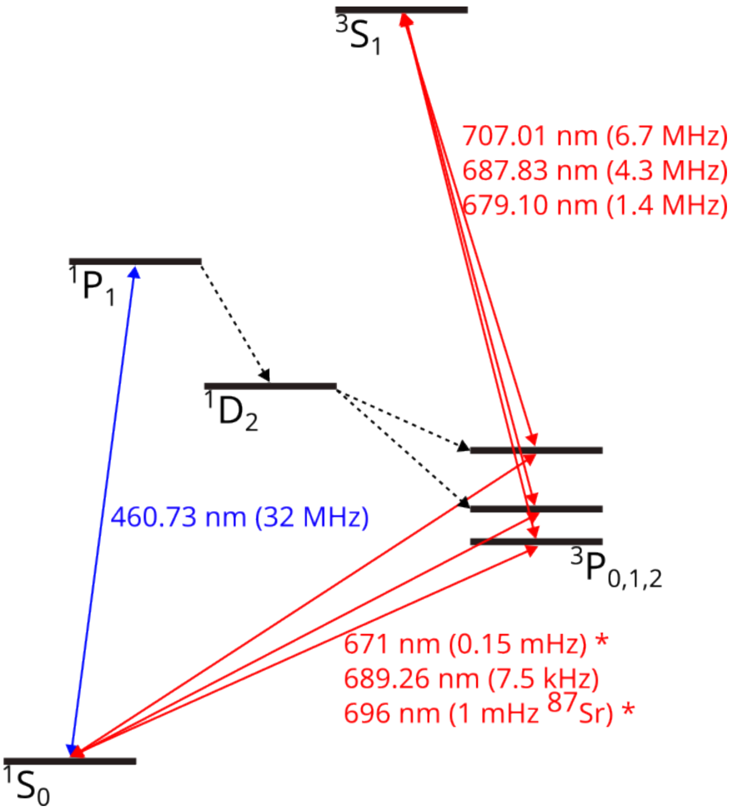

Figure 1 – Spectral lines of ^{88}Sr. Transition wavelength (transition width in terms of $\Gamma/(2\pi)$).

Source: By the author.

Among the motivations for choosing ^{88}Sr isotope are those related to the electronic structure depicted in Figure 1 with data from KRAMIDA and POLI (35, 36). One of the advantages is the fact the fundamental level ($^1S_0$) has zero magnetic dipole moment ($J = 0$), thus making it insensible to magnetic field perturbations. Furthermore, the structure exhibits several narrow and ultra-narrow resonances between the singlet ground state and the triplet ^3P_J states, inter-combination lines with applications in laser-cooling, and definition of clock transitions. Last but not least, the short s-wave scattering length of ^{88}Sr (37) avoids collisions between atoms, which can cause perturbative line shifts and broadenings. Indeed, strontium is one of the hottest candidates for the next-generation atomic clocks with unsurpassed stability and accuracy (38–41). Strontium optical lattice clocks operated on a magical wavelength (813 nm) were devised by YAMAGUCHI (38). Non-classical quantum correlation, such as spin-squeezing (40), super-radiant clocks, and lasers (39, 42) have been investigated and strontium-based experiments aimed at testing fundamental laws of physics have been designed (41, 43, 44). Lastly, many laboratories worldwide have developed strontium atomic interferometers (21, 42, 44, 45).

A particularity of our approach is the use of a laser-pumped optical ring cavity with which atoms interact in several ways. (i) Tuned far from the red side of atomic resonances, the intra-cavity light exerts attractive forces on the atoms, maintaining them trapped within the cavity mode volume, where they can, in principle, interact with all incident light fields for arbitrarily long times. (ii) The light fields injected into the cavity are resonantly enhanced by orders of magnitude and their frequencies are precisely defined by the cavity's resonances (46). (iii) In a certain regime, called 'bad cavity' limit and strong collective coupling, the coupled atom-cavity dynamics become non-linear and develop bi-stability, as demonstrated in this dissertation. (iv) The particular geometry of a ring cavity offers interesting possibilities for the non-destructive monitoring of matter-wave trajectories, as experimentally demonstrated in SLAMA and BUX (47, 48) and theoretically applied for the detection of Bloch oscillations in SAMOYLOVA (49, 50). The reason lies in the fact two counter-propagating cavity modes have independent photon budgets only in a ring cavity, in contrast to a linear cavity. Therefore, the back-scattering process by an atom in a ring cavity preserves momentum, since the back-scattered light travels in the counter-propagating mode, with respect to the mode of the absorbed photon. In other words, the atomic motion is monitored via balance of photon numbers in the modes observed via fraction of photons leaking through the cavity mirrors without disturbing the atoms, since the time of response of our cavity is much longer than that of the transition (more details are provided in Section 3.4). As illustrated in Figure 2, our ring cavity is composed of three mirrors (51, 52).

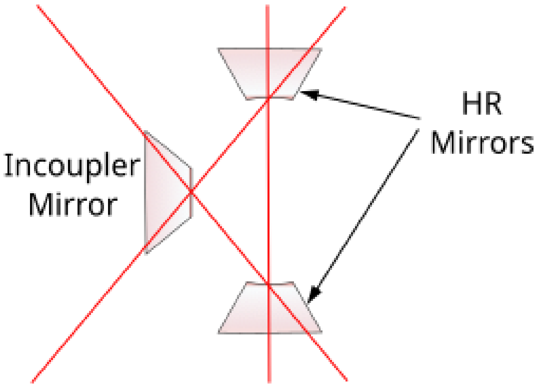

Figure 2 – Cavity with identification of mirrors (HR - *high reflection*) and the positions in which light can enter and exit.

Source: Adapted from RIVERO (53).

This dissertation is divided into five chapters, namely, introduction, Chapter 2, which reports the mathematical abilities necessary for the understanding of both subject and experiment, Chapter 3, which describes the functioning and the requirements for the development of interferometry, Chapter 4, which provides the results achieved and published during this master program with the experiment in a regime outside of resonance

(*Normal-mode splitting* (54)), as well as possible outputs, and Chapter 5, devoted to the achievements and projections for future paths.

1.2 Why quantum sensing using cavities?

Up to this point, the idea of quantum sensing was explored with the use of cavities due to their inherent advantages. Building a sensor involves obtaining a device, module, or subsystem that can detect changes in the environment and transmit the information to a processing system. Therefore, improving sensors is essential for achieving measurements with greater sensitivity and accuracy.

A quantum sensor uses quantum correlations, like entanglement, to enhance both sensitivity and resolution. Among quantum sensors, atoms are noteworthy due to their intrinsically quantum nature and variety of energy levels, which enable work with ultra-narrow transitions. They are employed as atomic clocks and gravimeters, providing exceptional precision attributable to the longer lifetime of ultra-narrow transitions.

The construction of a quantum sensor requires the exploration of strategies (*e.g.*, spin-squeezing technique) that maximize the signal-to-noise ratio and employ entanglement among atoms for surpassing the Standard Quantum Limit and approaching the Heisenberg Limit. Given our focus on developing a quantum sensor for gravimetry, the atoms must respond to the gravitational force. This can be achieved with the use of light and optical cavities aligned with the direction of gravity.

An advantage of using cavities is the possibility of extracting information such as spontaneous emission of atoms via the light transmitted, since the light that enters the cavity can exit the optical cavity only at a rate determined by κ, where κ is called linewidth of the cavity. Consequently, the information is extracted from the atoms and sent for further processing, as depicted in Figure 3.

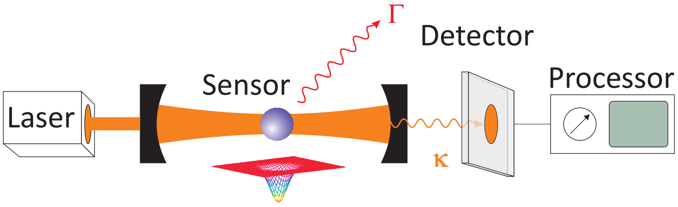

Figure 3 – Illustration of sensing using an optical cavity.

Source: By the author.

Strontium was cooled and placed inside the ring cavity, which was pumped by both a resonant laser with respect to the cavity and a red detuned laser related to atomic transition ${}^1S_0 \rightarrow {}^3P_1$. The cavity transmission T is detected at a frequency relative to its linewidth κ, as illustrated in Figure 4 and with the laser pumping at a η rate. In what follows is the explanation, in qualitative terms, of the motivation for our experiment and the reason why it was designed to operate in the 'bad-cavity' limit.

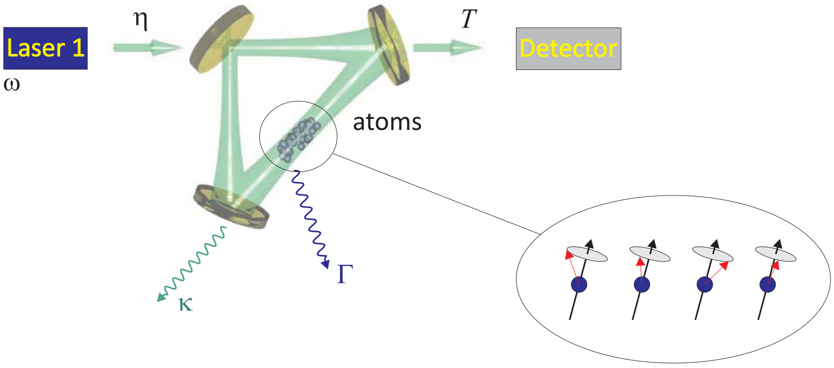

Figure 4 – Main scheme of our experiment. According to the inset, even if the atoms are in the same state, their spins remain uncorrelated.

Source: By the author.

Since our sensor is supposed to be quantum, a quantum description must be provided. The light field is described by a photon annihilation operator $\hat{a}$ and the atoms are expressed by two-level quantum systems, *i.e.*, spins represented by vectors of Pauli matrices $\hat{\mathbf{s}} = \frac{1}{2}\hat{\vec{\sigma}}$. In the absence of contact interactions, the atomic spins sum up to a total collective spin $\mathbf{S} = \sum_j \hat{\mathbf{s}}_j$ following the rules of the SU_2 algebra of angular momenta. The model is called Dicke model, represented by the Hamiltonian,

$$\hat{H} = -\imath\eta\left(\hat{a} - \hat{a}^\dagger\right) + g\left(\hat{S}_+\hat{a} + \hat{a}^\dagger\hat{S}_-\right),$$

where $\hat{a}$ and $\hat{a}^\dagger$ are annihilation and creation operators, η is the pumping rate, g is the coupling constant, and $\hat{S}_\pm = \hat{S}_x \pm i\hat{S}_y$.

Driven by a light field, a single spin (also called qubit) always evolves (in the absence of spontaneous emission) on the surface of a so-called Bloch sphere. When several spins are coupled, the total spin ends up on one of various concentric spheres, as illustrated in Figure 5. The important point is once the collective spin points to a specific Bloch sphere, no coherent collective evolution can change it, since $\hat{H} = \hat{H}(\hat{\mathbf{S}})$ depends only on the collective spin and $[\hat{\mathbf{S}}^2, \hat{\mathbf{S}}] = 0$. Consequently, all atoms initially in the ground state correspond to a fully stretched collective spin state, which remains despite being excited by a light field.

The fact spins are fully stretched does not mean they are correlated. Figure 4 illustrated it by arbitrary precession angles for individual spins. The linear terms in the Hamiltonian can only perform rotations of the collective spin. The correlation of spins, *i.e.*, spin-squeezing, which is a weak form of entanglement, requires non-linear terms in the interaction Hamiltonian, *e.g.*, terms quadratic in the z-component of the collective spin. In bad-cavity limit, the spontaneous emission Γ is negligible, due to excited atoms

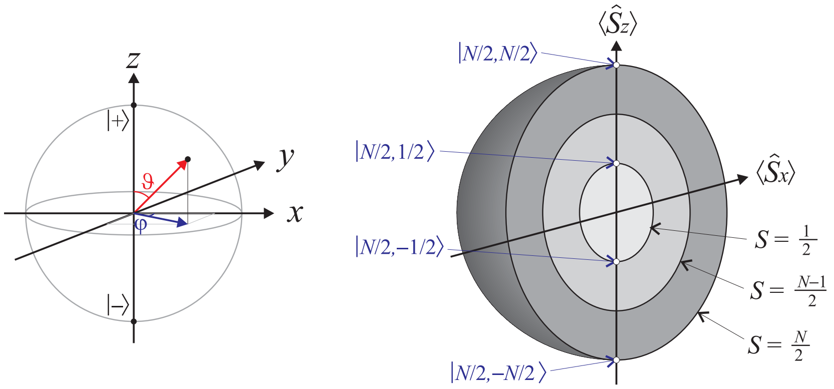

Figure 5 – (left) Single two-level atom Bloch sphere. (right) Collective Bloch sphere for N non-interacting atoms where the total spin is equal to the sum of all spins. Consequently, the Bloch sphere for the spin will be the collective Bloch sphere with a ratio equal to $\frac{1}{2}N$ ratio.

Source: By the author.

delivering their photons into the cavity mode via stimulated emission. However, in the strong collective coupling regime, the stimulated photon emitted has a good chance to be reabsorbed by another atom before being sent away from the cavity at a κ rate. Such a photon exchange between atoms can lead to non-classical correlations.

The time scale for the evolution of the cavity light field is given by κ and Δ_c, which is the detuning of the cavity with respect to the atoms ($\Delta_c = \omega_c - \omega_a$). If $\kappa \gg \Gamma$, then the time scale is dominated by κ, *i.e.*, the cavity fields evolve so fast that they follow the action of the collective atomic spin is doing. In other words, the light field is no longer an independent parameter, thus being slaved to the atomic dynamics. It may be removed from the Hamiltonian by a process called adiabatic elimination. The resulting Hamiltonian is

$$\hat{H} \simeq U\hat{S}_+\hat{S}_- \ ,$$

where $\hat{S}_+\hat{S}_- \simeq \hat{S}_z^2$ for large atom numbers and U is a constant that depends only on experimental parameters, *i.e.* on κ and Γ, detunings Δ_c and Δ_a (which is the detuning of the laser with respect to the atoms, $\Delta_a = \omega_L - \omega_a$), and cavity pump rate η.

The observation of signatures of the presence of such non-linearities in the bad-cavity Hamiltonian is the goal of our experiment, described in the next subsection.

2 THEORETICAL FUNDAMENTALS

After grasping the significance of quantum sensing, as elucidated in Chapter 1, the necessity of a comprehensive theoretical framework rooted in quantum mechanics is evident. This framework emphasizes the domains of radiation-matter interaction and matter-wave interferometry. Books on Quantum Mechanics, Radiation-Matter Interaction, Interferometry, and Electromagnetism (51, 55–62) are recommended for studies of the subjects presented here.

As reported in Section 1.1, the studies will focus on resonant systems, such as matter interferometer and Bloch oscillations. The theoretical arguments are divided into concepts of wave-matter interferometry (Section 2.1), type of interferometer to be implemented in the experiment (Section 2.2), and a brief introduction of Bloch oscillations (Section 2.3).

2.1 Matter-Wave Interferometers

Matter-wave interferometers use diffractive beam splitters - the light shift potential, akin to a periodic scattering potential, can be idealy defined as a potential influenced by light. In a broader context, it considers an effective wave vector $\vec{k}_e$, as outlined in (62). The potential is described as

$$V(\vec{r}) \propto |e^{i(\vec{k}_e\cdot\vec{r}+\varphi)} + e^{i(-\vec{k}_e\cdot\vec{r}+\varphi)}|^2 = ... \tag{2.1}$$

where ω_e and $\vec{k}_e$ represent the effective frequency and wave vector felt by the atoms, respectively, and φ is the phase. Term "effective" is employed because the direction of atom *i.e.* motion and the direction of light propagation must be considered in function of type of transition to be performed.

Let us consider a two-level atom, with $|a\rangle$ as the ground state and $|b\rangle$ as the excited state with energies E_a and E_b, respectively. Resonance frequency ω_0 is such that the energy difference between the states is $\Delta E = E_b - E_a = \hbar\omega_0$. The momentum transfer in the system is quantized, gaining or losing an integer multiple of the recoil momentum, thus resulting in a transfer of $\pm\hbar\vec{k}_e$, governed by Bragg condition for momentum conservation:

$$\vec{k}_e \cdot \left(\vec{p}_0 + \frac{\hbar}{2}\vec{k}_e\right) = 0, \tag{2.2}$$

where $\vec{p}_0$ is the initial momentum of the atom. Therefore, when a beam of atoms with momentum $\vec{p}_0 = \hbar\vec{k}_0$ in state $|a\rangle$ (denoted as $|a, \vec{p}_0\ \rangle$) is scattered by a spatially periodic potential generated by two counter-propagating waves of same frequency ω_L, two different states, namely, $|a, \vec{p}_0\ \rangle$ and $|b, \vec{p}_0 + \hbar\vec{k}_e\rangle$ are produced, as illustrated in Figure 6.

Since the atoms scatter due to the periodic potential, two groups of atoms are separated by a momentum difference of $\hbar\vec{k}_e$. Notably, atoms will absorb only one photon

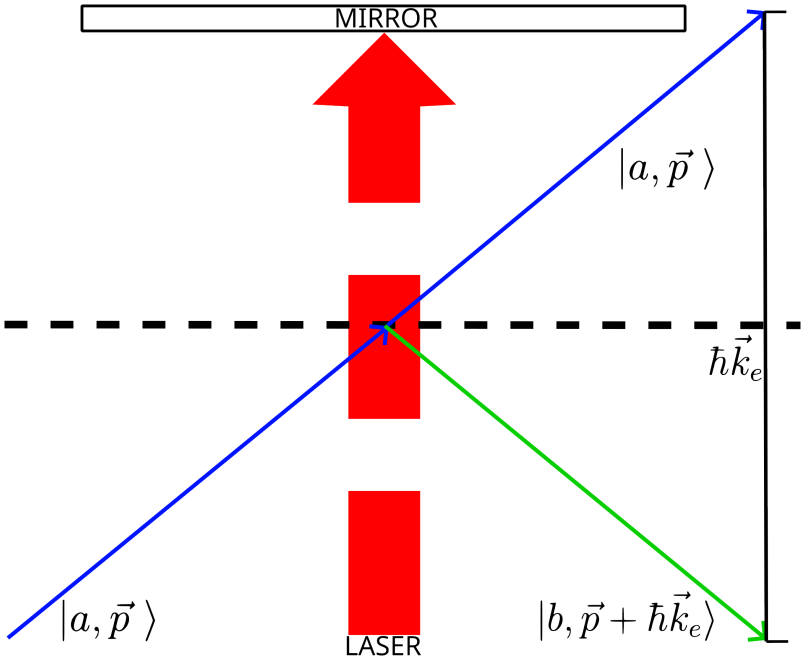

Figure 6 – Scattering of matter interacting with one of the two waves generated by the laser reflected by the mirror.

Source: By the author.

from one of the two waves, for absorbing a second photon would trigger stimulated emission, resulting in no momentum transfer to the atom. This fact also explains why atoms can acquire only $\pm\hbar\vec{k}_e$, where the sign indicates which of the two waves was absorbed.

Let us now examine effective quantities $\vec{k}_e$ and ω_e, which vary in function of type of transitions. As an example, in a pure two-level system, $\omega_e = \omega_1 + \omega_2$, and $\vec{k}_e$ follows a similar pattern. However, for a cascade two-photon transition with co-propagating waves, $\omega_e = 2\omega$ and $\vec{k}_e = \vec{0}$, whereas for the standing-wave case (first-order Bragg diffraction), $\omega_e = 0$ and $\vec{k}_e = 2\vec{k}$. In general, the wave vector can be described as $\vec{k}_e = \vec{k}_1 + \vec{k}_2$, where $\vec{k}_1$ and $\vec{k}_2$ refer to each field with which the atom can interact.

The system can be described by Schrödinger representation in a laboratory frame, with Rotating Wave Approximation (RWA), resulting in

$$i\hbar\frac{\partial}{\partial t}\vec{\Psi}(\vec{r},t) = \left[-\frac{\hbar^2}{2M}\vec{\nabla}^2 + \hat{H}_0 + \hat{H}_1\right]\vec{\Psi}(\vec{r},t), \tag{2.3}$$

where $\vec{\Psi}(\vec{r},t)$ is the system's wave function, which can be split into two parts, I and II, before and after the periodic potential

$$\vec{\Psi}(\vec{r},t) = \begin{bmatrix}\vec{\Psi}_{II}(\vec{r},t)\\ \vec{\Psi}_{I}(\vec{r},t)\end{bmatrix},$$

and the two Hamiltonians are free system Hamiltonian $\hat{H}_0$ and interaction Hamiltonian

$\hat{H}_1$. The former is given by $\hat{H}_0 = \frac{E_a+E_b}{2}\hat{\sigma}_0 + \frac{\hbar\omega_0}{2}\hat{\sigma}_z$, where $\hat{\sigma}_0$ is the identity matrix and $\hat{\sigma}_z$ is Pauli matrix. The interaction Hamiltonian, in a matrix form, is

$$\hat{H}_1 = \begin{bmatrix} V_{bb} & V_{ba} \\ V_{ab} & V_{aa} \end{bmatrix},$$

and the potential terms are related to the electric dipole Hamiltonian, such that $V_{ab} = V_{ba}^* = -\hbar\Omega U(\vec{r},t)e^{-i\left(\omega_e t - \vec{k}_e\cdot\vec{r}+\varphi\right)}$, where Ω is the Rabi frequency of the two-level atom and $U(\vec{r},t)$ is the field envelope, a quantity playing a crucial role in interferometry. For V_{bb} and V_{aa}, the type of two-level system adopted must be considered. In general, it is proportional to the product of the field envelope with its complex conjugate divided by the difference between levels $U(\vec{r},t)U^*(\vec{r},t)/\Delta\omega$ (62).

Rabi frequency is a quantity that defines the oscillation frequency of probability amplitudes between two levels and can be mathematically described in different ways. Two forms are described here, *i.e.*, its main derivation from a quantum system that interacts with a field such as $\hat{H}_1$ and the use of the concept of cross-section $\sigma(\omega)$.

The derivation of the former is simple (63) and results in the fact Ω is proportional to transition dipole moment $\mu = e\vec{r}$, where $\vec{E_0}$ is the interacting electric field and $\hat{\mu}$ is the dipole moment operator such that $\hat{H}_1 = \hat{\mu}\cdot\vec{E}$ and

$$\Omega_R = \frac{\langle\vec{\Psi}_a|\hat{\mu}\cdot\vec{E_0}|\vec{\Psi}_b\rangle}{\hbar}, \tag{2.4}$$

where an index referring to the transition to systems with more than two levels can be used, *i.e.* Ω_{ab}. However, since our system will be a two-level one, it is simpler to use only Ω_R.

For the second case, related to Equation 2.4, since intensity I of a laser is proportional to the square of the electric field, then (57)

$$\Omega_R^2 = \sigma(\omega_0)\frac{I}{\hbar\omega_0}\Gamma, \tag{2.5}$$

where Γ is the width of the transition used and $\sigma(\omega_0)$ cross-section can be described in terms of wavelength λ and transition width Γ, such that (57)

$$\sigma(\omega_L) = \frac{g_2}{g_1}\frac{\lambda^2}{2\pi}\frac{\frac{1}{4}\Gamma^2}{\left(\Delta^2+\frac{1}{4}\Gamma^2\right)}, \tag{2.6}$$

where g_1 and g_2 are the degeneracies of lower and upper states, respectively, and $\Delta = \omega_L - \omega_0$ is the detuning, *i.e.*, the difference between laser frequency ω_L and transition frequency ω_0.

The calculations provided in Appendix A of Equation 2.3 lead to two equations that will determine the operation of the system considering momentum, *i.e.*,

$$\begin{aligned}&\left[\frac{\hbar^2}{2M}\left(\vec{K}^2+\vec{k}^2\right)-\frac{p^2}{2M}+V_{bb}+\hbar(\omega_0-\omega_L)\right]u_{b,\vec{k}}(\vec{p})-\hbar\Omega u_{a,0}(\vec{p})=0,\\ &-\hbar\Omega u_{b,\vec{k}}(\vec{p})+\left[\frac{\hbar^2\vec{K}^2}{2M}-\frac{p^2}{2M}+V_{aa}\right]\hbar\Omega u_{a,0}(\vec{p})=0,\end{aligned} \tag{2.7}$$

which is the formalism that describes the system after passing through the periodic potential created by the laser, represented in Figure 6 by the red arrow, which is reflected by the mirror. Wave functions $u_{a,0}(\vec{p})$ and $u_{b,\vec{k}}(\vec{p})$ are the solutions of Equation 2.3, from the method of separation of variables successively, as in Appendix A, and eigenfunction $\vec{\Psi}(\vec{r},t)$ is expressed as

$$\vec{\Psi}(\vec{r},t)=e^{-i(\omega t+\varphi)\frac{\sigma_z}{2}}\begin{bmatrix}e^{i(\vec{K}+\vec{k}_e)\cdot\vec{r}} & 0\\ 0 & e^{i\vec{K}\cdot\vec{r}}\end{bmatrix}\begin{bmatrix}u_{b,\vec{k}}(\vec{p})\\ u_{a,0}(\vec{p})\end{bmatrix}e^{-i\frac{E}{\hbar}t}. \tag{2.8}$$

Equation 2.7 claimed the operation of the type of interferometer to be implemented must be determined. An example of a matter interferometer is Ramsey-Bordé interferometer, whose construction is the same of Mach-Zender-type interferometers and will be studied in Section 2.2.

2.2 Ramsey-Bordé Interferometer

The way a Mach-Zender-type interferometer works must be initially understood so that the type of interferometer under analysis can be performed. Starting from the idea two beams of light can interfere with each other based on a phase difference acquired by travelling different paths, a beam splitter is used in a way incident light can generate two beams of light with same characteristics (*e.g.*, frequency and coherence). The observation of interference requires intensities and polarization of those two split beams (separated in a beam splitter) be maintained equal and recombined with another beam splitter. Both interference pattern and phase difference generated by the path difference are observed, thus leading to our Mach-Zender interferometer for light.

Similarly to light interferometry, an analogous interferometer for matter waves (64) can be built using Bragg pulses, which are two counterpropagating beams with a 2Δ difference of frequency, where Δ is the detuning of the laser with relation to the atomic transition. Figure 7 presented the structure of this interferometer, which, instead of working with light and the difference between paths, works with matter wave and the phase difference is created due to the transfer of momentum to the atoms through light pulses, represented by red and green arrows. Figure 7 also describes states considering our transition as Raman. Such an interferometer uses temporal evolution to lead to two different momentum states that will interfere with each other.

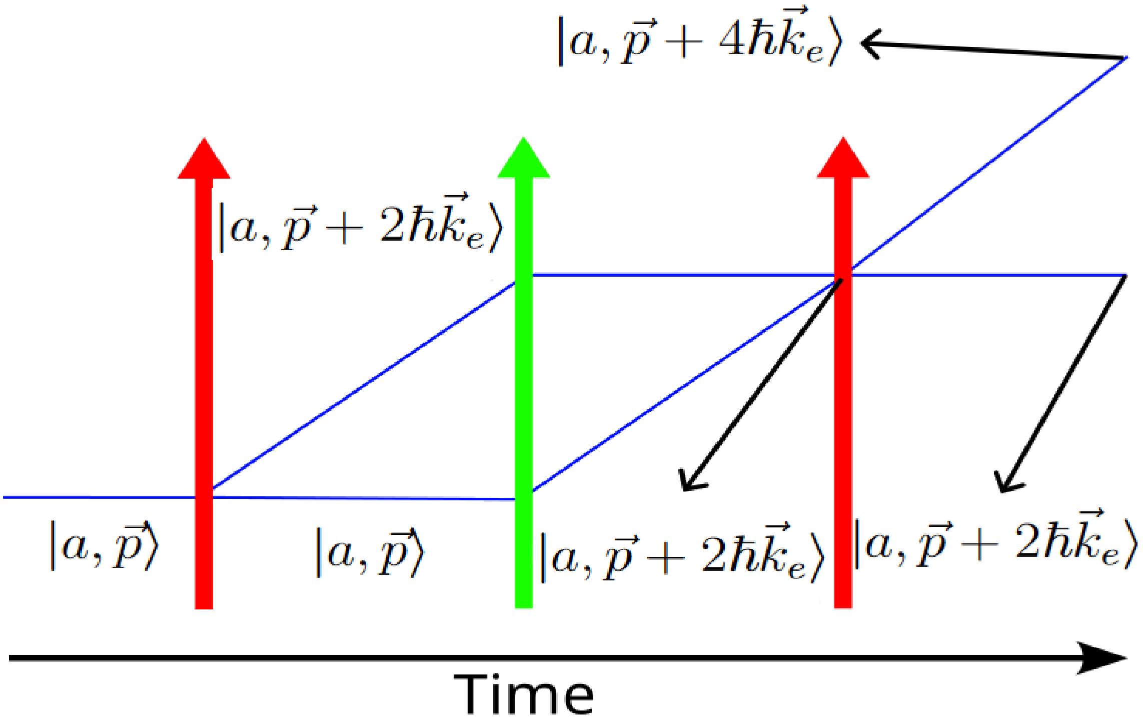
$|a, \vec{p} + 4\hbar\vec{k}_e\rangle$
$|a, \vec{p} + 2\hbar\vec{k}_e\rangle$
$|a, \vec{p}\rangle$
$|a, \vec{p}\rangle$
$|a, \vec{p} + 2\hbar\vec{k}_e\rangle$
$|a, \vec{p} + 2\hbar\vec{k}_e\rangle$
Time

Figure 7 – Ramsey-Bordé Interferometer. Red and green arrows represent $\pi/2$ and π pulses, respectively, and the described states show the transfer of momentum after each pulse starting from an initial state $|a, \vec{p}\rangle$. Black arrows indicate the location of such states. The time between the pulses is T', which is necessary for the occurrence of temporal evolution. In general, momentum is given by vector $\vec{p}$; however, only one direction is normally chosen (p_z).

Source: By the author.

The light pulses determine an important part of interferometry and must be adjusted with $\pi/2$ and $\pi-$pulses defined by relation $\frac{\pi}{2} = \Omega\Delta t$ and $\pi = \Omega\Delta t$, respectively, where Ω is Rabi frequency and Δt is the pulse duration. The parameters that undergo adjustments are pulse duration Δt - the duration of the sequence in the experiment control could be controlled - and Rabi frequency Ω. Their physical representation and the operation of the interferometer can be performed through the Bloch sphere, shown in Figure 8.

The description of Bloch sphere, which uses the interaction picture, shows the first pulse shifts the initial state of momentum $|p_z\rangle$ to a superposition state of states $|p_z\rangle$ and $|p_z + 2\hbar k_e\rangle$, both in ground level $|a\rangle$, since we are working with Raman transition. The evolution time, *i.e.*, the interval between pulses, adds phase difference to our system, which is very important for interference. The phase accumulated by an arbitrary momentum state $|\vec{p}\rangle$ is given by

$$\phi_p = \frac{1}{\hbar}\int_0^T E dt, \tag{2.9}$$

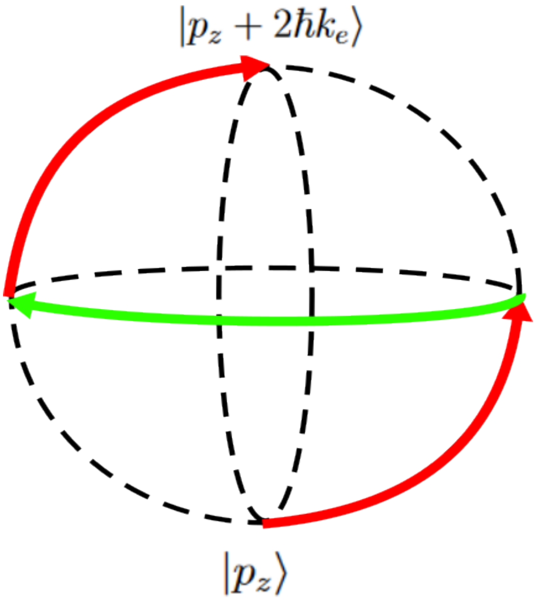

Figure 8 – Bloch Sphere. The three pulses used for interferometry, with a $\pi/2-$pulse in red, creating initially a superposition state, and a $\pi-$pulse in green, generate a temporal evolution in the superposition and adding phase. Towards finishing the sequence, a second $\pi/2-$pulse sends the atoms to one of the two states. Interference occurs with atoms that finish in the same level, but with a different path - some of them will be in state $|p_z\rangle$ after the first $\pi/2-$pulse and others will be in $|p_z + 2\hbar k_e\rangle$, *i.e.* in a superposition of both states.

Source: By the author.

where E is the system's energy and T is the total experiment time.

In the second pulse, *i.e.*, $\pi-$pulse, the populations are inverted, *i.e.*, atoms in state $|p_z\rangle$ go to state $|p_z + 2\hbar k_e\rangle$ and those in $|p_z + 2\hbar k_e\rangle$ go to $|p_z\rangle$, keeping the system in a superposition state, but adding a phase. The orientation of the π-pulse relative to the $\pi/2$-pulse is crucial in determining the momentum description during the second pulse and establishing the necessary conditions. Such an inversion can be seen in Figure 8 as the rotation of Bloch vector by π *rad* on the Bloch sphere.

After the temporal evolution, the last pulse of the sequence, *i.e.*, another $\pi/2-$pulse is performed, causing the Bloch vector to rotate $\frac{\pi}{2}$ *rad*. It can act in two different ways, one on each state. Since the superposition state between $|p_z\rangle$ and $|p_z + 2\hbar k_e\rangle$ has a group of atoms in each of them, $\pi/2-$pulse can cause part of the atoms to go to each of states $|p_z\rangle$ and $|p_z + 2\hbar k_e\rangle$, separating them into only two groups. Atoms that completed the path in $|p_z + 2\hbar k_e\rangle$, but transitioned through $|p_z\rangle$ during the π-pulse, will interfere with atoms that also reached $|p_z + 2\hbar k_e\rangle$, but passed through $|p_z + 2\hbar k_e\rangle$ during the π-pulse. Such interference creates a phase difference between the atoms, which is critical to the overall behaviour of the system.

As a result for the entire series of pulses and the plane wave solution that considers the interaction with the acceleration of gravity, the momentum evolves with time so that $p = p_n + mgt$, where p_n is the atom's momentum such that $p_n = n\hbar k_e$ with $n \in \mathbb{Z}$, which represents the quantumness of our system, and mgt, which works classically. Here, momentum $\vec{p}$ is worked only in the direction parallel to gravity, *i.e.*, $z-$axis. Therefore, the phase accumulated during the entire experiment is $\Delta\phi = \phi_{|b\rangle} - \phi_{|a\rangle}$, where phases $\phi_{|b\rangle}$ and $\phi_{|a\rangle}$ are related to the wave function that resides in states $|b\rangle$ and $|a\rangle$, respectively. As shown in Figure 7, the momentum for those two states will be $p_z = p_0$, $p_z = p_2$, and, with the action of gravity, $p_z = p_2 - mgt$. Towards a clearer understanding, let us consider the conditions under which an atom can acquire a quantum momentum of $2\hbar k_e$ while losing classical momentum equivalent to mgt.

More than one momentum can exist within a same state, since not all atoms in initial state $|a, \vec{p}\rangle$ will acquire momentum by the end of the pulse sequence, thus leading to two distinct states, namely, $|a, \vec{p}_0\rangle$ and $|a, \vec{p}_2 - m\vec{g}t\rangle$. The phase in each state will be the sum of the phases of atoms in the same state with different momenta

$$\phi_{|a\rangle} = \phi_{p_0} + \phi_{p_2 - mgt},$$
$$\phi_{|b\rangle} = \phi_{p_2} + \phi_{p_2 - mgt}.$$

and using Equation 2.9, the phase difference is

$$\Delta\phi = \frac{kg}{2}t^2 + \omega_{rec}t, \tag{2.10}$$

where $\omega_{rec} = E_{rec}/\hbar$ is the recoil frequency. Index n in the momentum is an internal characteristic of the atom and, therefore, can be used for writing the state with level and momentum index $|\alpha, n\rangle$, where α is ground state a or excited state b. With this notation, the initial momentum is considered zero $p_0 = p_{n=0} = 0$. The state previously represented as $|a, \vec{p}_0\rangle$ is now $|a, 0\rangle$ and, similarly, for the excited state, $|b, 1\rangle$. In this case, the total momentum is only on $z-$axis.

2.3 Bloch Oscillations

A different matter-wave interferometric technique is based on the observation of Bloch oscillations, whose theoretical description must initially consider the Hamiltonian of a one-dimensional system interacting with a periodic potential $V(x)$, such that $V(x) = V(x + m\ell)$ with $m \in \mathbb{Z}$ and where ℓ is the periodic spacing of the potential. Our analysis found a system characterized by energy band gaps, where each discrete energy level may correspond to a continuous quasi-momentum, as illustrated in Figure 9.

Atoms must acquire kinetic energy through an external force and oscillate in a way to achieving Bloch oscillations. Since they gain kinetic energy due to gravitational force, oscillation is generated by the absorption of momentum through interaction with a light

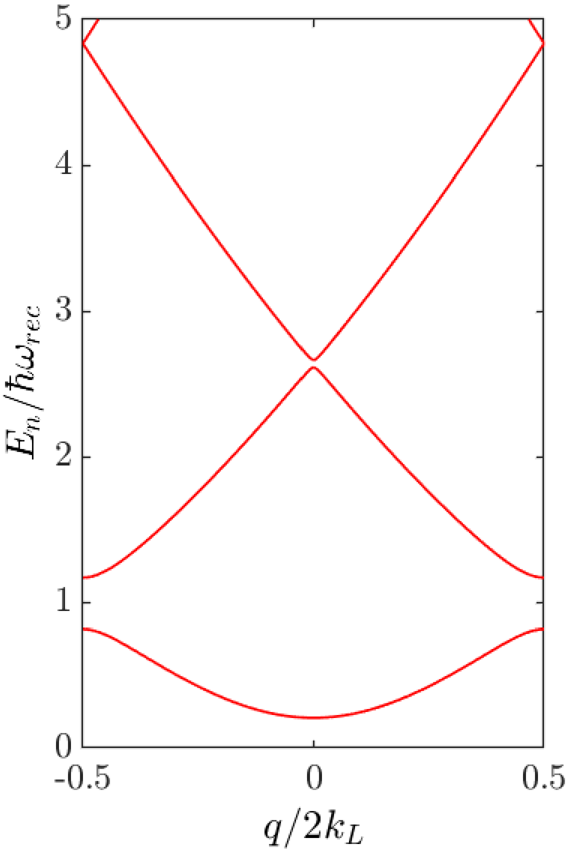

Figure 9 – Energy bands in a system with periodic potential.

Source: By the author.

beam. Here, a resemblance between Bloch oscillations and Ramsey-Bordé interferometer (Section 2.2) is observed, since momentum gain from light interaction occurs discretely for momentum gains that are integer multiples of $\hbar k_e$.

A relation must be established between momentum and the external force of a system confined in a periodic potential. Since the momentum presented so far is discrete, the concept of quasi-momentum q is adopted such that

$$\frac{\partial \vec{q}}{\partial t} = \frac{\partial \vec{q}_0}{\partial t} + \vec{F}_{ext}, \tag{2.11}$$

where q_0 is the initial quasi-momentum and external force $\vec{F}_{ext}$ in our experiment is given by the gravitational force, such that $\vec{F}_{ext} = m\vec{g}$.

Therefore, Bloch oscillations arise because the atom can acquire momentum from the periodic lattice and the external force will act in the opposite direction, creating oscillation, which can be directly derived, considering an electron, by equation

$$\hbar \frac{d\vec{k}}{dt} = -F_{ext}, \tag{2.12}$$

by determining the velocity of the system as a function of the wave vector, its position can be derived in one dimension, $v(k) = \frac{1}{\hbar}\frac{dF}{dk}$, therefore,

$$x(t) = \int v\left(k(t)\right) dt, \tag{2.13}$$

resulting in an oscillation in position with $\omega_{\text{Bloch}} = aF/\hbar$ angular frequency, where a is a lattice parameter. Since $a = \lambda_L/2$, which represents the periodic lattice formed in a cavity by two counter-propagating beams, we can derive a system oscillation frequency that is proportional to the external force, given by

$$\nu_{Blo} = \frac{mg}{2\hbar k}. \tag{2.14}$$

For more details, readers are invited to consult the solid-state literature, which introduces Bloch theory, Brillouin zones, and related topics (65–68).

3 EXPERIMENT

This chapter describes an experiment and its operation aimed at quantum sensing, as cited in Chapter 1, specifically applied to gravimetry, and outlines the procedures for implementing the pulses of Ramsey-Bordé interferometer (Section 3.5 and Section 4.2). For more details on the experimental description, please refer to (53, 54, 69–71).

Regarding the description of the setup, shown in Figure 10, the system can be divided into three main parts, namely, blue system, red system, and science chamber. Blue and red systems refer to the preparation of the light used for the operation of the gravimeter, which is located in the science chamber (third system).

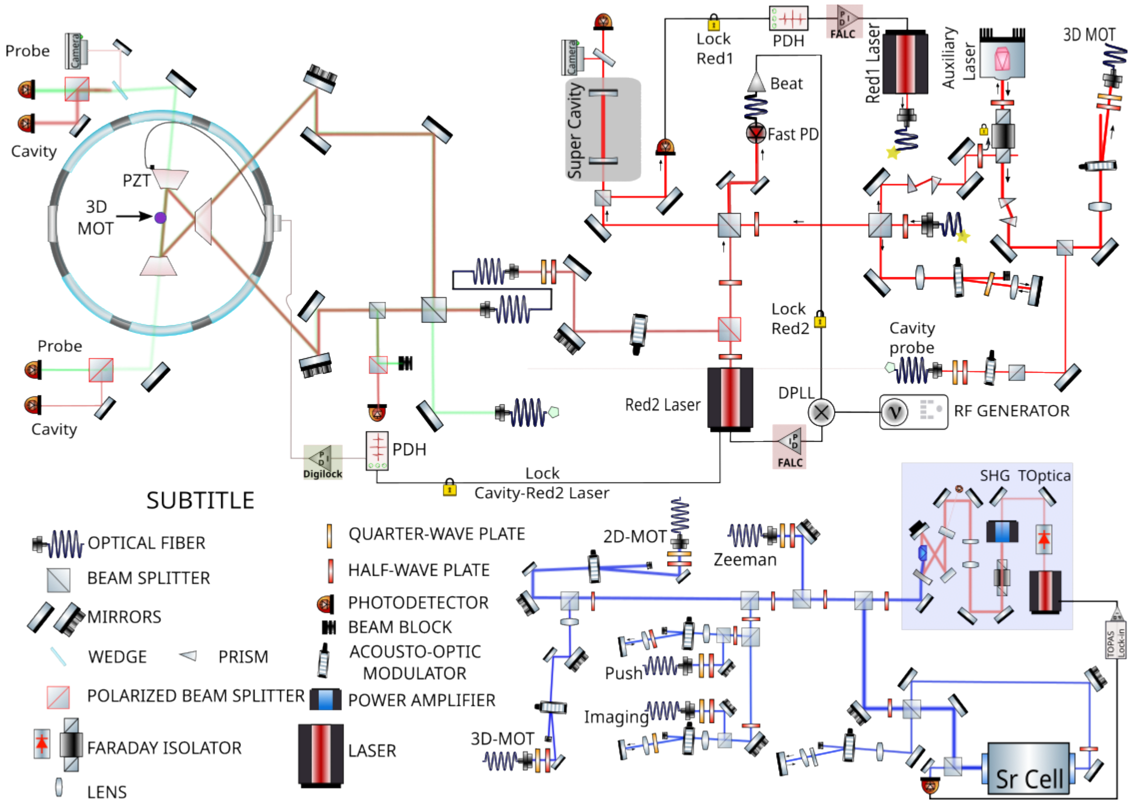
Probe
Camera
Cavity
PZT
3D MOT
Probe
Cavity
Camera
Super Cavity
Lock Red1
PDH
FALC
Red1 Laser
Auxiliary Laser
3D MOT
Beat
Fast PD
Lock Red2
Cavity probe
Red2 Laser
DPLL
RF GENERATOR
FALC
PDH
Digilock
Lock Cavity-Red2 Laser
SUBTITLE
OPTICAL FIBER
BEAM SPLITTER
MIRRORS
WEDGE
PRISM
POLARIZED BEAM SPLITTER
FARADAY ISOLATOR
LENS
QUARTER-WAVE PLATE
HALF-WAVE PLATE
PHOTODETECTOR
BEAM BLOCK
ACOUSTO-OPTIC MODULATOR
POWER AMPLIFIER
LASER
2D-MOT
Zeeman
SHG
TOptica
TOPAS Lock-in
Push
Imaging
3D-MOT
Sr Cell

Figure 10 – Complete experimental setup.

Source: Adapted from RIVERO (53).

The experiment required a ring cavity with its main axis aligned parallel to the axis perpendicular to the ground so that external force F_{ext} could act on the cold strontium atoms to be the gravitational force. The geometry of the ring cavity can be seen in Figure 2.

In what follows is the preparation of the systems and their respective functions, including all processes for stabilizing the light, frequency difference, power control, and most of the experiment's control circuits.

3.1 Blue System

The Blue System, introduced in Figure 11, features a single blue laser and was divided into three sub-systems, namely, spectroscopy, 2D Magneto-optical Trap (push, Zeeman, and 2D trap), and Science Chamber, of which the latter contains all components that lead to the science chamber, including light for absorption imaging and 3D MOT (Magneto-optical Trap).

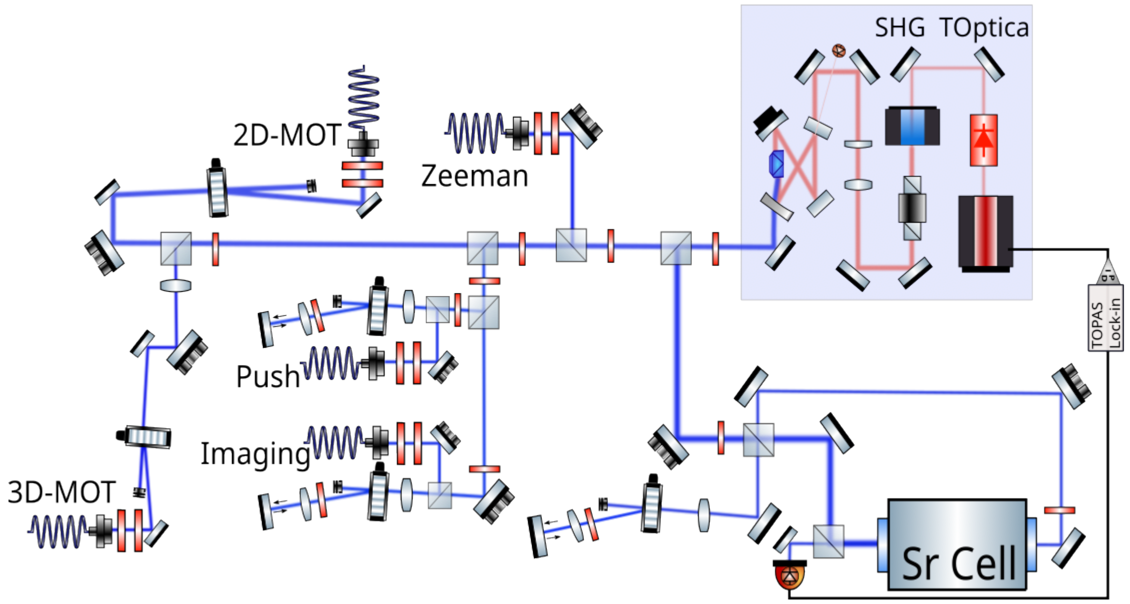

Figure 11 – Blue System.

Source: Adapted from RIVERO (53).

The blue laser is generated via second harmonic generation and is commercially available. Consequently, all locking systems are part of an internal program provided by the equipment supplier (TOPAS Lock-in). A saturated absorption signal must be sent to the blue laser system so that the laser can be locked at the desired frequency. The signal is generated in a strontium cell maintained at approximately 580 K, ensuring strontium is in a gaseous form. The operation of the experiment is similar to that of (OK?) the dispersive curves described in Section 3.2; however, a saturated absorption signal instead of a reflection one is used.

In the spectroscopy part, the saturated absorption probe beam passes through a double pass AOM (Acoustic-optic Modulator) at $+130$ MHz, ensuring the blue laser is locked to blue transition $^1S_0 \rightarrow {}^1P_1$ (461 nm) with a detuning equivalent to that frequency - it is equivalent to the Blue laser being locked at -130 MHz of the blue transition (red detuned).

Regarding 2D MOT, two fibers receive significant power (Zeeman beams: 30 mW; 2D MOT: 40 mW) - precautions must be taken due to the sensitivity of the blue fibers to high intensities. Zeeman beams, *i.e.*, the Zeeman slower system (72, 73), trap atoms with higher velocities in the 2D MOT, thereby increasing the number of atoms sent to 3D MOT. Zeeman beams can trap faster atoms because of their higher detuning in comparison to 2D MOT beams, which pass through a double-pass AOM directed from spectroscopy with a $+105\ MHz$ frequency shift, leading to a detuning of $\Delta_{461nm} = -30.96\ MHz$.

In the push mechanism, the beam that transfers atoms from 2D MOT to 3D MOT, located in the Science Chamber, passes through a double-pass AOM at $+72.04\ MHz$. The setup exerts a force on the trapped atoms, directing them along the push path until they encounter the 3D MOT and are trapped again in the Science Chamber.

Finally, 3D MOT passes through an AOM at $+100\ MHz$, resulting in a $\Delta_{461nm} = 35.96\ MHz$ detuning. Such light is further divided and prepared, since the polarizations for 3D MOT are crucial for efficient trapping. Consequently, the last blue laser beam applies to the absorption imaging method, which involves capturing two images, *i.e.*, one with atoms and the imaging light and another with only this light. In the first image, atoms absorb the light, causing less light in the systems where atoms are present. The subtraction between the images produces a third image depicting the position of our atomic cloud, as shown in Figure 12. Such a sequence for imaging is necessary only for measurements in 3D Red MOT and for the atoms trapped in the ring cavity. It is also used for quantifying the atoms present in Blue MOT and for tracking the position of our clouds.

3.2 Red System

The Red System works with light from transitions ${}^1S_0 \rightarrow {}^3P_1$ and those used as re-pumpers (${}^3P_{0,2} \leftrightarrow {}^3S_1$). Figure 13 described the entire light preparation system; all apparatuses are necessary for the construction of a gravimeter due to factors such as low natural linewidth $\Gamma_{689nm} = 7.1\ kHz$, leading to higher precision of the gravimeter. Some tools maintain both precision and stability of the system, which is necessary for reaching the transition of low natural linewidth.

Figure 13 provided stabilization mechanisms such as super-cavity, beat, and injection system, of which the former is a commercial optical cavity with two mirrors and bandwidth, κ, of $1.54\ kHz$.

The reflection signal from that super-cavity was used for the preparation of a lock-in that employs FALC (Fast PID from *Toptica*) circuit and PDH (Pound-Drever-Hall) technique. The circuit uses the reflection signal, performs a derivative, and obtains the dispersion signal, which enables sending a correction signal to the laser proportional to the distance from the lock-in position. The signals are provided in Figure 14.

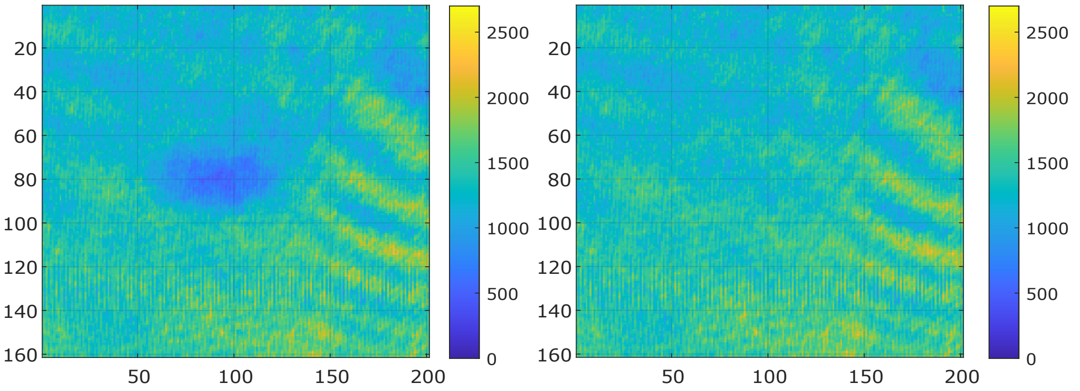

(a) With atoms

(b) Without atoms

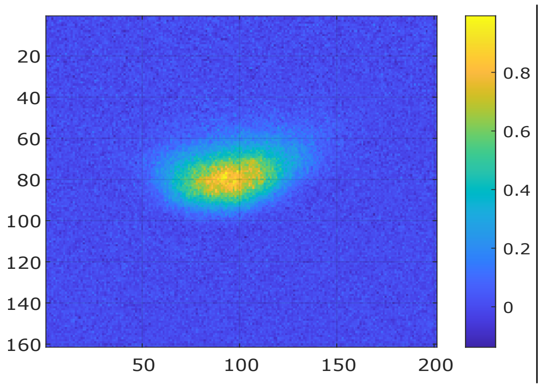

(c) Optical density image

Figure 12 – Absorption images taken (a) with atoms – consequently, an absorption shadow is present; (b) without atoms - the image contains all information of our imaging beam (including distortions in the profile) - note the scale goes up to 2600, which relates to the pixel depth of our camera (12bits); and (c) optical density resulting from the subtraction of the images. A dark image containing information on the camera noise was also used; however, it is not relevant for the understanding of the principle.

Source: By the author.

The super-cavity with the locking system can lock the Red 1 laser, which is employed to lock all light necessary for performing 3D red MOT and the cavity light, which constitutes our periodic potential $V(z)$. The cavity light is generated by Red 2 laser, which is locked by a beat between it and Red 1. Therefore, a fast photo-detector will sense small changes between one laser and another.

Both lasers (Red 1 and 2) must have a predetermined frequency to ensure a correct beat. Although the locking system is similar to the use of dispersion curves, locking is performed by a DPLL (Digital Phase-Locked Loop) (74). A VCO (Voltage-Controlled Oscillator) signal enables comparing the circuit's frequency to the frequency difference in the beat, which is the difference between the frequencies of Red 1 and 2.

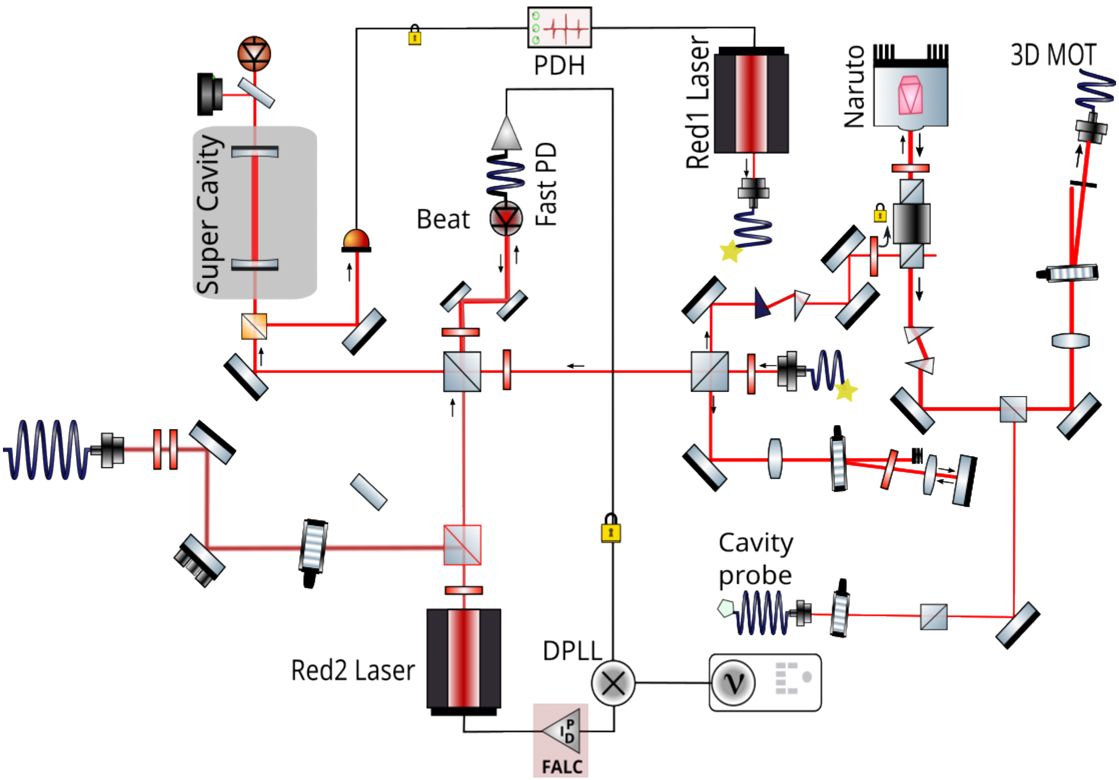

Figure 13 – Red System.

Source: Adapted from RIVERO (53).

The circuit determines the way Red 2 (cavity laser) changes compared to Red 1, which is locked in the super-cavity. It provides a signal in DPLL that is sent to a second FALC that communicates the correction signal to Red 2. Therefore, the annular cavity laser is stabilized via beat.

Finally, the laser used for creatign our 3D MOT at ${}^1S_0 o {}^3P_1$ transition operates at a 689 nm wavelength. Therefore, a diode laser was specifically built to enable injection locking (69). Injection is a process through which the light from a master or primary laser, with a Q_1 quality factor, is injected into a diode of a second or auxiliary laser, with a $Q_2 < Q_1$ quality factor. When the system's mode matches, *i.e.*, when the spatial shape and polarization of both lasers are close enough, one of the second laser's modes is amplified, so that the amplified frequency is resonant with the mode of the light from the primary laser.

The auxiliary laser was therefore locked and the system stability was established according to a primary reference that does not significantly change over time. Our super-cavity and Red 1 laser enable determining the stability of Red 1 laser and the frequency necessary for achieving our 3D red MOT, with the auxiliary laser serving as the light for it. However, the cavity's resistance used for obtaining the temperature inside the cavity

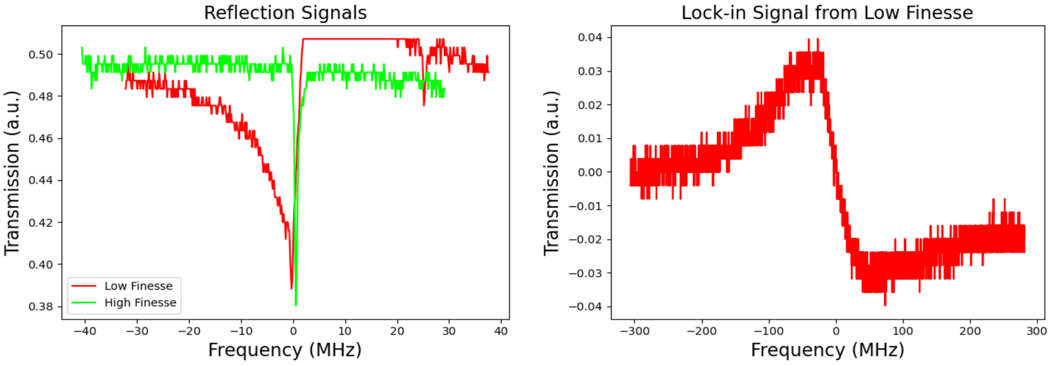

(a) Reflection signal of ring cavity (b) Dispersive curve of Lock-in

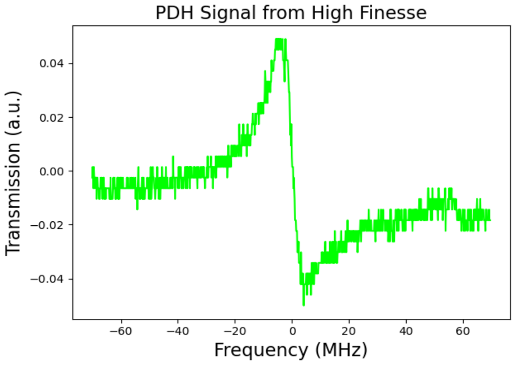

(c) Signal of the PDH

Figure 14 – Signals of lock methods of Lock-in and PDH. (a) A full scan of the piezo from the ring cavity shows the two spectra for both finesses. Reflection valleys are reallocated for comparisons. (b) and (c) are signals after the circuits of Lock-in and PDH, respectively.

Source: By the author.

continuously measured by a multimeter and the RF frequency that determines the MOT position must be taken into account. Even with changes in the super-cavity position, the way to rediscover the red MOT can be indicated, since it cannot be observed with the naked eye due to its narrow transition width. For more details on MOT, please refer to Section 3.3.1 and previous studies conducted by the group (53, 69, 70). Since an auxiliary laser is a highly intense diode laser, part of its power is also used as a probe beam in experiments conducted for NMS measurements (54).

Now, let us revisit Figure 13 to identifying the frequency relations used in our experiment, since the light for MOT should not have the exact frequency of the chosen transition. An AOM with a frequency shift of +80.00 MHz is applied to the auxiliary laser utilized in the 3D red MOT. Simultaneously, another portion of the auxiliary laser, designated for probing, passes through a separate AOM also set at +80.00 MHz. Finally, the last AOM, operating at a radio-frequency (RF) value of +100.32 MHz, is dedicated to the ring cavity laser (Red 2). All AOMs in the experiment operate at +1 diffraction order, which implies they are always in the blue shift of the transition.

Besides changing frequency, the AOMs in the experiment also function as a type of shutter, since when the sending of the RF signal is interrupted, AOM stops diffracting the light. Consequently, the light that passes takes a different path and cannot follow the same trajectory as the diffracted order. As a result, the light prepared in the Red Part continues its path to the Science Chamber through optical fibers.

3.3 Science Chamber

In this compact system, the incoming light undergoes significant modifications primarily in its polarization, which serves the dual purpose of achieving trapping and measurement objectives. Additionally, the light's power is regulated by PBS (Polarized Beam Splitters) and half-wave plates, ensuring a precise control over the light's properties for optimal performance. Overall, the entire system can be visualized through Figure 15. Due to the complexity of the area, it will be subdivided into two parts, namely, MOTs (Section 3.3.1) and Ring Cavity (Section 3.3.2).

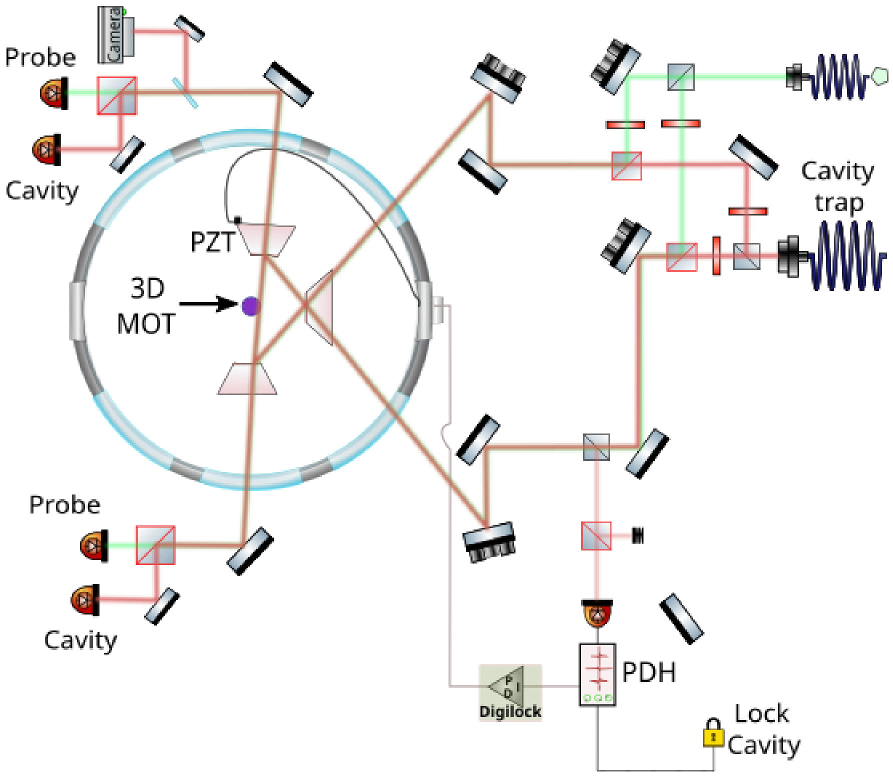

Figure 15 – Science chamber System with cavity trap laser and probe laser separated by polarization.

Source: Adapted from RIVERO (53).

3.3.1 3D Blue and Red MOT

Our experimental procedure of cooling begins with the implementation of a MOT, which is critical for cooling and trapping atoms and, in its absence, atoms would not be cold enough to remain confined within the ring cavity. The blue MOT, operating at transition ${}^1S_0 \rightarrow {}^1P_1$ with 461 nm wavelength, works to reducing the temperature of the atoms arriving from 2D MOT to around 10 μK. Since this is still not cold enough for the atoms to be trapped in the periodic potential, further cooling is required using the red transition (${}^1S_0 \rightarrow {}^3P_1$), which can achieve temperatures of the order of 800 nK.

Setting up the red 3D MOT is not as straightforward in comparison to the blue MOT. A frequency oscillation for trapping the fastest atoms, due to the Doppler effect, as well as a power ramp must be generated so that most atoms are trapped in this new trap, as shown in Figure 16. The ramp enables the capture of atoms with higher energy, which are farther from resonance due to the Doppler effect. The final frequency value of the red MOT is determined by the super-cavity. Therefore, stability of the super-cavity is crucial, since the red MOT will be observed only at that frequency, which remains constant for the atoms, but changes over time in our reference frame due to fluctuations in the super-cavity.

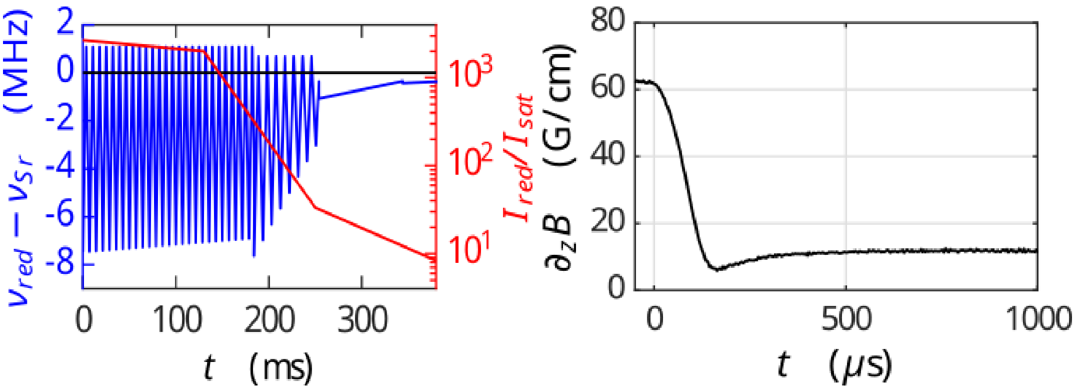

(a) Frequency and Intensity (b) Magnetic Field

Figure 16 – Signal showing the operation of 3D red MOT, with frequency and power ramp necessary for trapping a larger quantity of atoms. (a) frequency oscillation to trap the fastest atoms due to Doppler effect in blue and power ramp in red. (b) magnetic field during the transference of atoms from blue MOT to red MOT.

Source: Adapted from RIVERO (53).

Power distribution and polarization for both MOTs are prepared in an intermediate section between the Science Chamber and the red and blue systems, as illustrated in Figure 17. Dichroic mirrors enable the combination of blue and red lights into a single path and also introduce the red light from transitions ${}^3P_{0,2} \rightarrow {}^3S_1$, which act as repumpers.

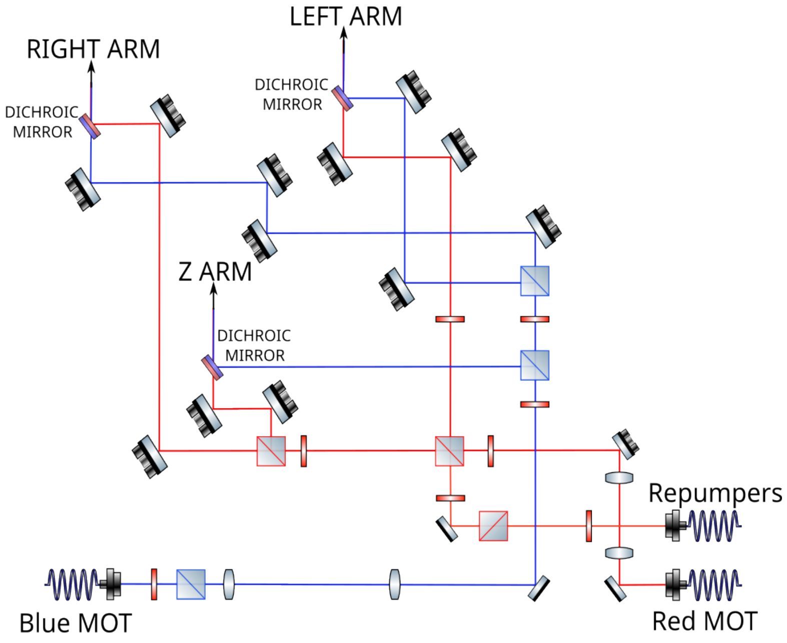

Figure 17 – Apparatus for power balancing, alignment, polarization, and repumpers of blue and red MOTs, resulting in the three arms of MOT.

Source: By the author.

The re-pumpers work by bringing atoms back to ${}^3P_1$ state, enabling them to remain trapped in MOT, which is necessary due to the probability of atoms in ${}^1D_2$ state transitioning to ${}^3P_2$ rather than ${}^3P_1$. Given the long lifetime of approximately $\sim 6666\ s$ in ${}^3P_2$ state, ${}^3P_1$ state must be repopulated.

A laser is added at ${}^3P_2 \rightarrow {}^3S_1$ transition. However, from the ${}^3S_1$ state, the atom can transition to either the desired ${}^3P_1$ state, or ${}^3P_{0,2}$, which requires the addition of another transition ${}^3P_0 \rightarrow {}^3S_1$. As a result, two re-pumpers operating at wavelengths of $707\ nm$ and $689\ nm$, corresponding to transitions ${}^3P_2 \rightarrow {}^3S_1$ and ${}^3P_0 \rightarrow {}^3S_1$, respectively, were incorporated. They repopulated the state that enables the atom to revert to the ${}^3P_1$ state, which is crucial for maintaining the desired atomic behaviour. It is noteworthy that the lifetime in the ${}^3P_0$ state is also quite long, i.e., approximately $(1000\ s)$, further emphasizing the importance of the re-pumpers in ensuring the stability and performance of the experimental setup.

Therefore, the MOT lights (blue, red, and repumpers) are directed to the inner part of the Science Chamber, where they will effectively trap strontium atoms.

3.3.2 Ring Cavity

The ring cavity used consists of three mirrors, as depicted in Figure 2, and two light fields coupled, namely, the light from the periodic potential and the probe light.

The operation of the system is illustrated in Figure 15. The two lights are distinguished leveraging their polarization and exploiting the property allowed by the ring cavity for polarization splitting. In other words, each polarization has two distinct bandwidths, represented by κ_s and κ_p. Perpendicular (s) and parallel (p) polarizations, each with its respective κ value are employed. The cavity design was made for $\kappa_s = 4$ MHz and $\kappa_p = 40$ MHz. Figure 18 displays the different κ values measured with the empty cavity, *i.e.* with no presence of atoms.

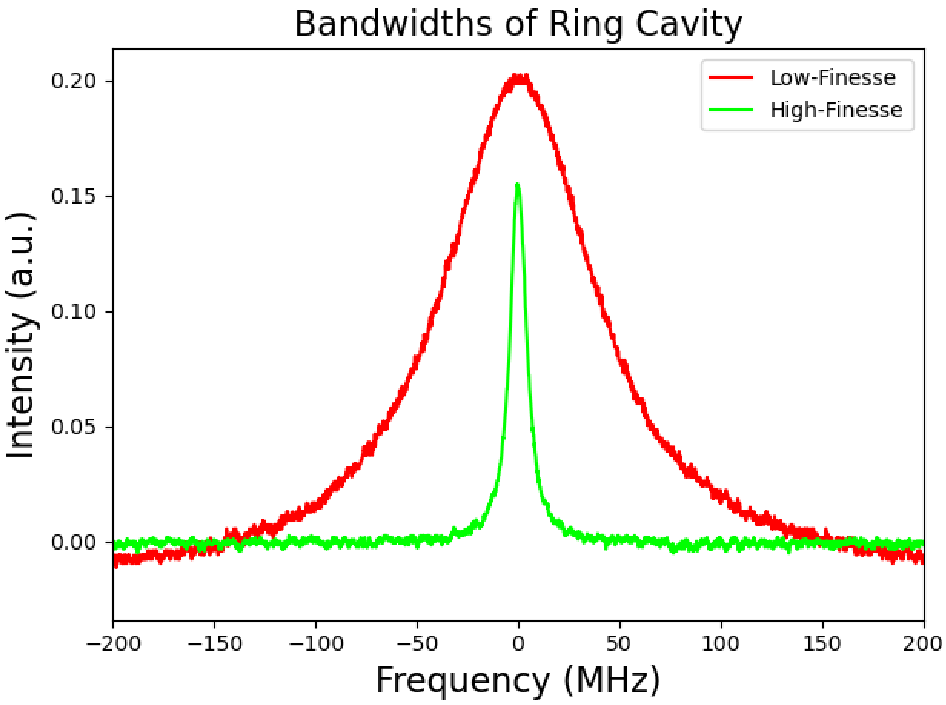

Figure 18 – Bandwidth κ for the two different polarizations, s (green curve) with $\kappa_s \sim 4$ MHz and p (red curve) with $\kappa_p \sim 40$ MHz, also called high and low finesse, respectively.

Source: By the author.

Again, Figure 15 shows several PBS designed for determining the input polarization and separating the polarizations exiting the cavity. The low power of the light exiting the cavity, ranging between ~ 60 μW and 150 μW, must be observed. At those intensities, external fluctuations can easily impact the experiment; therefore, the light passing through the cavity requires additional preparation given its importance and sensitivity.

3.4 High-coupling regime and normal-mode splitting

As addressed elsewhere, an experiment in which atoms interact via a narrow transition with a relatively bad cavity, $\kappa \gg \Gamma$, has been constructed. On the other hand, the operation could be maintained within the strong collective coupling regime, $g\sqrt{N} > \kappa$, where g is the single-photon Rabi frequency, also called atom-field coupling strength. In this limit, the collective coupling between atoms and cavity should lead to a splitting of the system's normal modes of $g\sqrt{N}$, which can be tested experimentally by recording cavity transmission spectra.

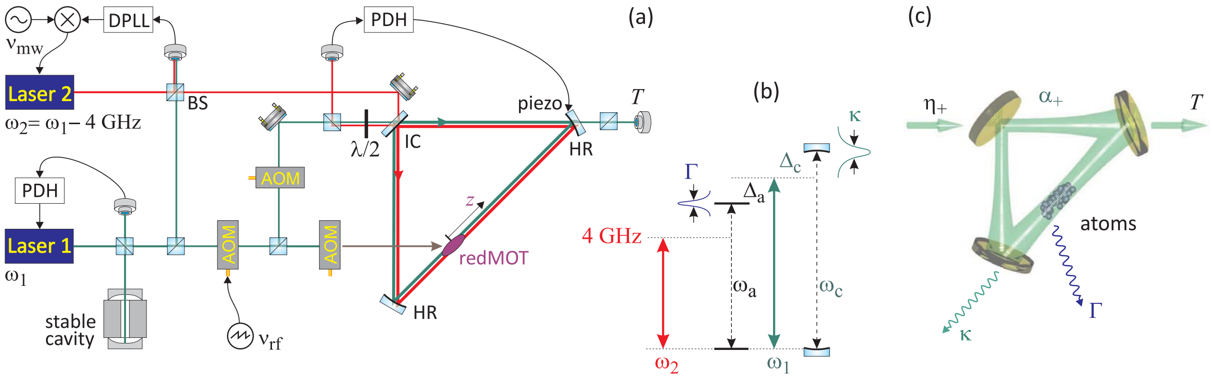

Figure 19 – (left) Laser scheme. (center) Detunings of the involved lasers (right) Scheme of the experiment.

Source: By the author.

When the laser frequency is tuned across a resonance frequency of the cavity, a peak whose width corresponds to the loss rate via transmission of light through the cavity mirrors is observed. A large cloud of strontium atoms was cooled to temperatures below 10 μK and then transferred into the cavity mode volume, where they are trapped by an optical dipole potential generated by two counterpropagating laser beams tuned $-4\ GHz$ below the atomic intercombination resonance, in the ${}^1S_0 \rightarrow {}^3P_1$ transition. Another laser beam is then injected into the cavity and tuned across resonance. The light transmitted through one of the cavity mirrors is recorded. The laser scheme is shown in Figure 19 [*] This is not so simple, since scanning a laser through a cavity resonance requires knowledge of the region where that resonance is placed, which is found only by injecting a laser for measuring the cavity length. This is performed with a second laser, which probes another cavity mode far from the atomic resonance not to perturb the atoms. Laser 2 actually confines the atoms in the cavity mode. Laser 1 is phase-locked to laser 2 and scanned to a cavity resonance, which is close to the atomic transition. The cavity itself can be adjusted employing a piezo..

The spectra observed are akin to those presented in Figure 20. A simple Airy profile is expected in the absence of atoms; however, the introduction of a cloud of ultracold atoms into the ring cavity leads to a notable transformation, i.e., the transmission peak splits into two, indicating presence of the atomic medium and its interaction with the cavity. Such normal mode splitting can be considered a smoking gun of the presence of atom-cavity interactions.

---

[*] .

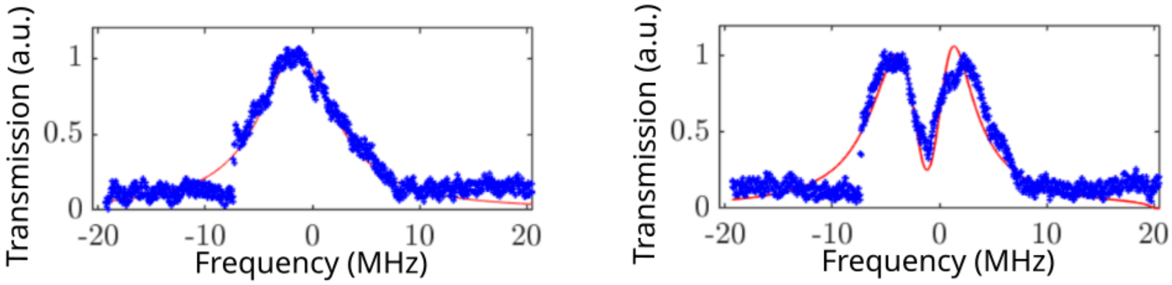

Figure 20 – (left) Cavity transmission spectra without atoms, (right) with atoms. Red curve is a fit considering only the region between $(-8, 8)$ MHz, which is the range of the probe scan.

Source: By the author.

However, NMS is not a quantum effect. Indeed, replacing the atoms by a classical beam splitter (as a *gedankenexperiment*) leads to the same normal mode splitting. This *gedankenexperiment* is possible because every atom acts like a beam splitter, reflecting some fraction of the incident light and transmitting the remaining one into the counter-propagating mode of the cavity without saturating our system, *i.e.*, in the linear optics regime.

The difference between atoms and beam splitters is atoms are saturable. This phenomenon serves as evidence of the quantum nature of our system, since saturation arises from the presence of a two-level system. The effect is a direct result of the discrete quantized energy levels exhibited by the atoms. Saturation leads to a non-linear behaviour, highlighting the intricate quantum dynamics at play within our system.

The non-linearity in the system arises from the fact that, when the laser crosses the resonance frequency ($\omega = \omega_c$), it strongly saturates the atoms. Therefore, it transfers half of the population to the excited atomic state, so that the effective atom number contributing to the normal splitting is drastically reduced, leading to an additional feature in the normal mode spectra near resonance (Figure 21).

3.5 Ramsey-Bordé Pulses Implementation

The implementation of the sequence of the three Ramsey-Bordé interferometry pulses, as presented in Section 2.2, requires the pulses shown in Figure 7 be accurately estimated. Equation 2.5 and Equation 2.6 show the area of our pulses is determined by product $\Omega\Delta t$, which is equal to π or $\pi/2$ for our pulses. The main factors that influence

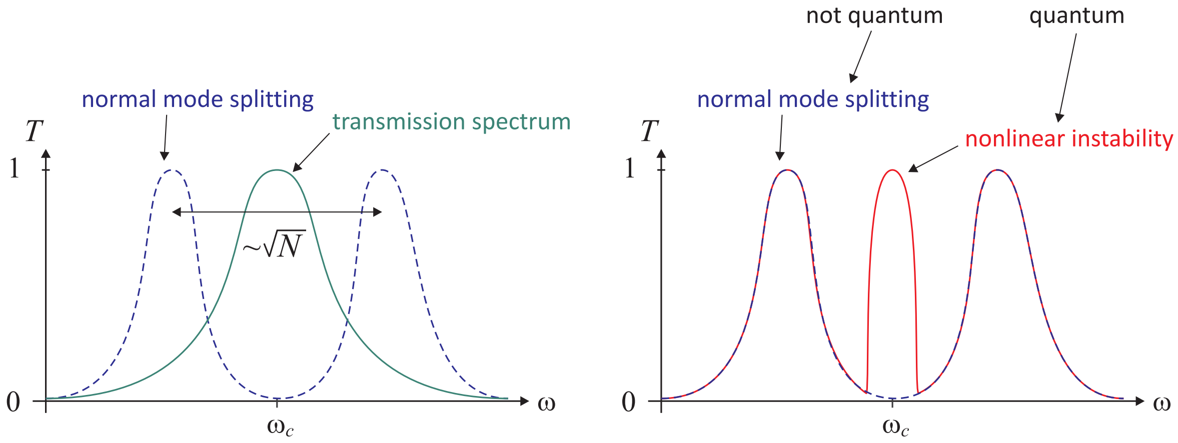

Figure 21 – (left) Classical normal mode splitting, (right) normal mode splitting in presence of a non-linearity near resonance.

Source: By the author.

this product are intensity I and detuning Δ, relative to the chosen transition with a linewidth of Γ.

Since intensity is equal to power per unit area, the value of I can be determined towards the obtaining of Rabi frequency, hence, the understanding of the pulse duration. Towards the development of pulse sequences for our project, a simulation estimated potential parameters that could be used in the experimental setup. The simulation, described in detail in Section 4.2, enabled the exploration of a range of possible parameter values and identification of those most promising for achieving our desired outcomes. It also considered the increase in light intensity due to cavity finesse, gravitational interaction during temporal evolution, varied temporal evolution times, and different values of g. As a result, the sequence of pulses can be experimentally tried with the use of two AOMs connected to a *National Instruments* board for the systematic control of the experiment. Such a control has a 0.02 ms minimum response time, which makes it our shortest possible pulse duration. For more details on the parameters for the pulse sequence, refer to Section 4.2.

4 RESULTS

This section provides some results for the non-linear normal mode splitting (Section 4.1) and simulations of the Ramsey-Bordé pulses sequence (Section 4.2) for estimating possible ways to experimentally do it.

4.1 Non-linear normal-mode splitting

The additional feature presented in Figure 21 shows the appearance of non-linearity caused by bi-stability displayed in Figure 22 and obtained by numerical calculations of normal mode spectra (ramping Δ_{ca}) for various detunings of the laser from atomic resonance (Δ_a), according to RIVERO (54). The horizontal cuts through the centre of the false colour images (near $\Delta_a = 0$) represent the normal mode spectra discussed in Section 3.4.

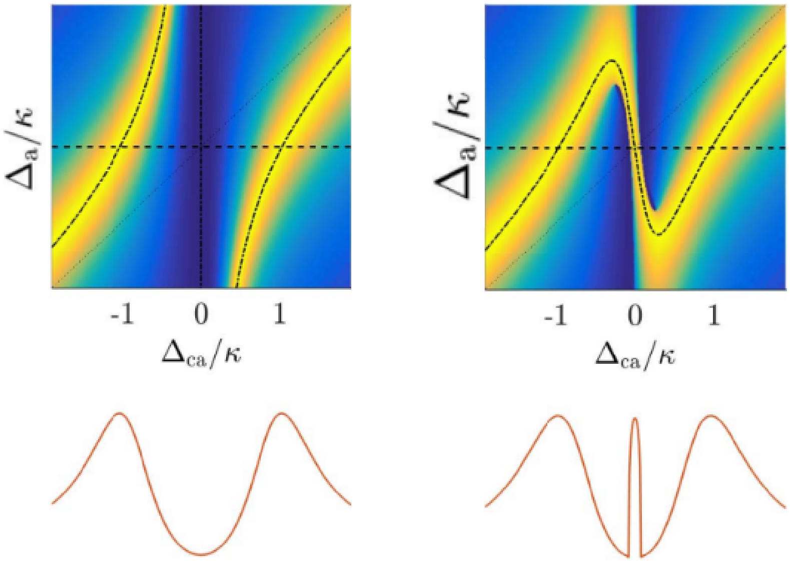

Figure 22 – (up left) Theoretical calculation of normal mode spectra without saturation effects, (upright) taking into account saturation effects and (down) signal for both cases with $\Delta_a = 0$ compared to Figure 21 and in ${}^1S_0 \rightarrow {}^3P_1$ transition.

Source: Adapted from RIVERO (54).

The ridges visible in the left figure represent the typical behaviour of an avoided crossing expected for a linear atom-cavity interaction. However, the experimental spectra (central figure) show an additional feature close to resonance ($\Delta_{ca} \simeq 0$), which can be explained only by a non-linearity. The sharp edges delimiting the centre ridge point to bi-stability. Indeed, the right figure shows theoretical curves calculated taking into account the saturation of the atomic resonance. The experimental spectra can be seen in Figure 23.

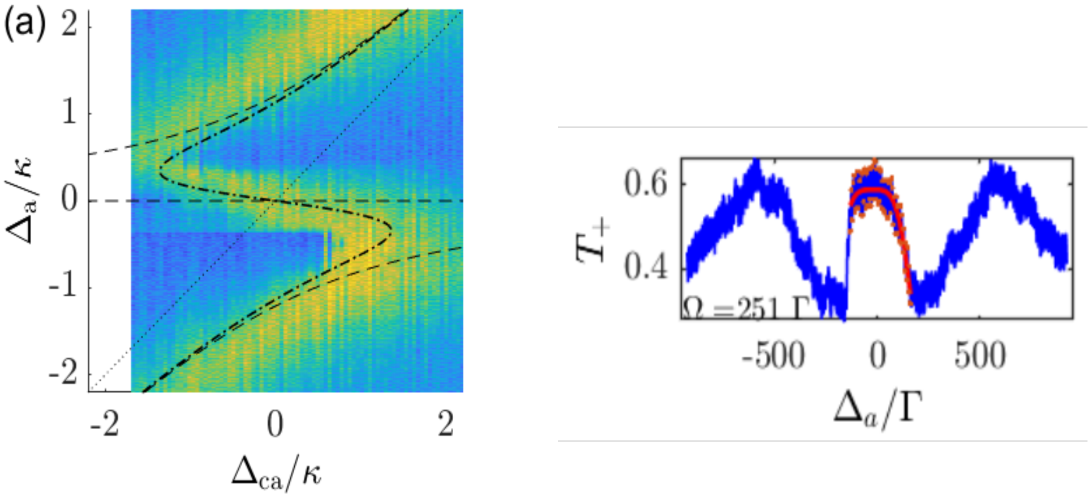

(a) Full scan of Δ_a

(b) Signal for one value of Δ_a

Figure 23 – (left) Experimental data of normal mode spectra with saturation effects using false colour image. Dashed line represents the numerical calculations provided in Figure 22. (right) Experimental data of one value of Δ_a for NMS, as expected.

Source: By the author.

The key takeaways from our observations are (i) bi-stability on a narrow resonance in the bad-cavity limit, which indicates presence of non-linearity in the system, and (ii) achievement of srong atomic saturation, corresponding to a 50% excited state population and suggesting the dynamics of the system are inherently quantum. Specifically, the quantum behaviour of a two-level system in saturation dynamics is observed. Taken together, those observations suggest the generation of non-classical correlations should, in principle, be possible within our system.

The relation of our non-linearity to pumping rate η shown in Figure 24 was also investigated. According to Figure 24, when power increases, the signal saturates and resembles a spectrum of an empty cavity. Such data were obtained setting one value of the probe laser power and varying the frequency of the probe, obtaining the signal displayed in Figure 23(b), thus showing our system has an important relation with saturation.

4.2 Numerical simulation of the sensitivity of Ramsey-Bordé pulse sequences

In the early nineties, KASEVICH and CHU (75) developed the technique of sensing external forces by matter-wave interferometry, introduced in the preceding chapters. In what follows is the estimation of its performance when applied to strontium atoms driving on their 7.5 kHz broad intercombination line ($^1S_0 \rightarrow {}^3P_1$). Such estimation is performed in two steps. First, the differential phase shift of an initially resting particle is derived following two different trajectories in a matter wave interferometer. The calculation is

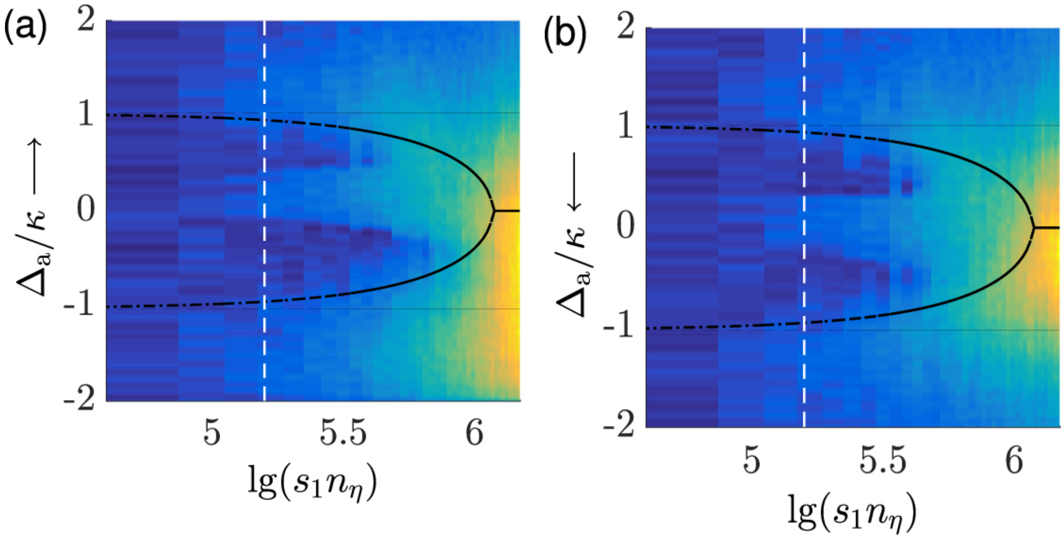

(a) Right direction scan (b) Left direction scan

Figure 24 – Intensity scan of NMS in false colour image. Increase in the power of the probe laser from left to right in both images. The distinction between them arises from the scanning direction, revealing a bi-stable behavior within our system. Moreover, the high saturation in the probe laser prevents observations of the NMS central peak.

Source: By the author.

then incorporated into a more general derivation of the expected Ramsey fringe patterns treating the atoms as individual two-level systems and taking into account their initial thermal velocity distribution.

A Ramsey-Bordé technique, similar to the setup shown in Figure 7, is explored, but with a focus on the influence of gravity as an external force. Such an alteration will impact the trajectory of the atoms traversing (OK?) both momentum states, illustrated in Figure 25. The effect of gravity on the atoms results in a momentum loss, which can be understood classically, as detailed in Section 2.2.

The pulse area in our pulse sequence is a critical consideration for ensuring the implementation of the two distinct types of pulses (π and $\pi/2$). A consistent pulse area can be maintained adjusting parameters, such as Rabi frequency Ω_R and pulse duration Δt. The concept is illustrated in Figure 26 for a π-pulse. Additionally, creating a $\pi/2$-pulse involves doubling pulse duration Δt, since product $\Omega_R \Delta t$ must equate to π or $\pi/2$, depending on the pulse type.

4.2.1 Phase shift in a Ramsey-Bordé interferometer

In what follows is the calculation of the time dependence of the dynamical phase accumulated by an atom in the field of gravity as a function of its initial momentum.

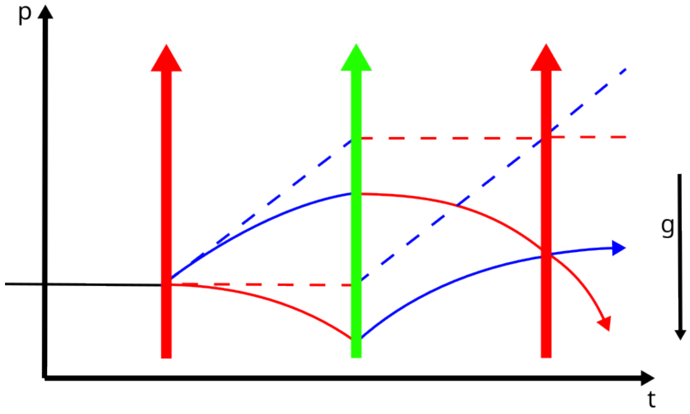

Figure 25 – Scheme of a Ramsey-Bordé interferometer considering gravity the external force acting only on $z-$axis, with the states presented in Figure 7.

Source: By the author.

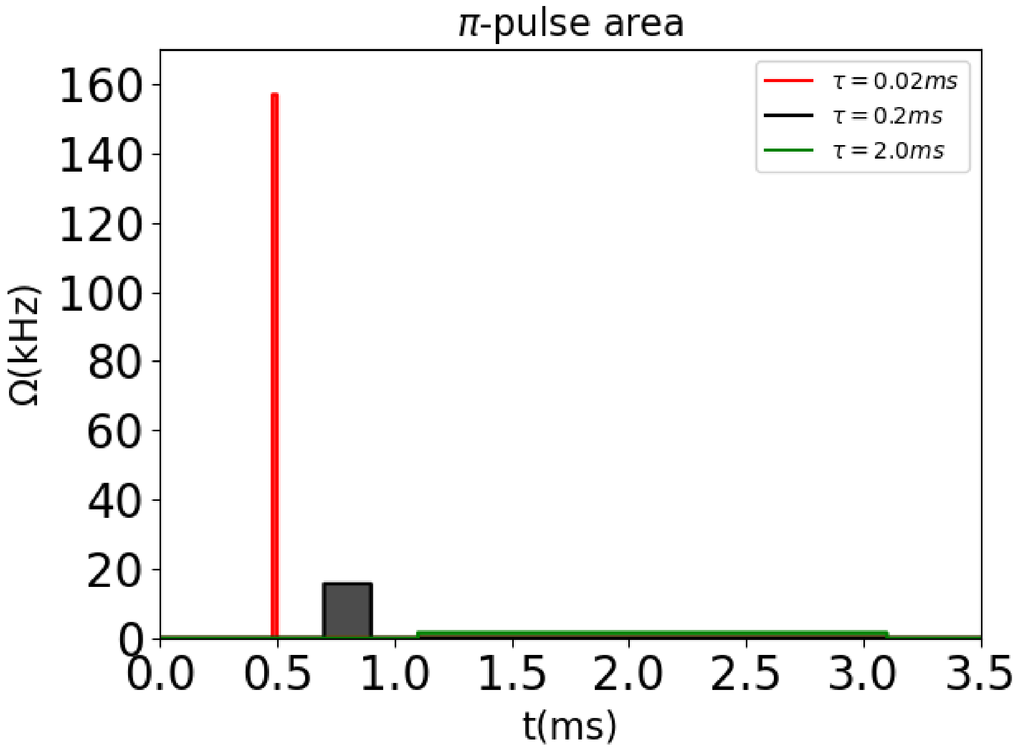

Figure 26 – A comparison among three π-pulses revealed higher intensity leads to increased saturation, whereas longer pulse duration results in greater interaction with gravity. The area of the pulse must remain constant.

Source: By the author.

Plane waves were considered, since any radial inhomogeneity in both atomic cloud and light mode within the cavity can be disregarded, thus facilitating the description of the system in a one-dimensional manner. The momentum evolves as

$$p = mgt + p_0. \tag{4.1}$$

Therefore, the accumulated phase is given by Equation 2.9, leading to

$$\phi_{p_0} = \hbar^{-1} \int_0^t E dt = \hbar^{-1} \int_0^t \frac{p^2}{2m} dt = \frac{mg^2t^3}{6\hbar} + \frac{p_0 g t^2}{2\hbar} + \frac{p_0^2 t}{2m\hbar}, \tag{4.2}$$

and the phase difference between the accumulated phase in the atoms that start with a momentum p_0 and that in the atoms that start with $p_0 = 0$ will be

$$\Delta\phi = \phi_{p_0} - \phi_0 = \tfrac{1}{2\hbar}(p_0 g t^2 + \tfrac{1}{m} p_0^2 t) \ . \tag{4.3}$$

For each of the two arms of a Ramsey-Bordé interferometer, *i.e.*, upper and lower ones, two contribution are calculated from the above result, *i.e.*, one phase shift accumulated between first and second laser pulses and another accumulated between second and third laser pulses,

$$\phi_{lower} = \phi_{p_0}|_{p_0=0} + \phi_{p_0}|_{p_0=\hbar k - mgt} \qquad \text{and} \qquad \phi_{upper} = \phi_{p_0}|_{p_0=\hbar k} + \phi_{p_0}|_{p_0=\hbar k - mgt} \ , \tag{4.4}$$

where t is the time interval between first and second laser pulses. Apparently, the phase shifts accumulated during the time interval between second and third laser pulses cancel out. Therefore,

$$\Delta\phi = \phi_{upper} - \phi_{lower} = \phi_{p_0}|_{p_0=\hbar k} - \phi_{p_0}|_{p_0=0} = \frac{\hbar k g t^2}{2\hbar} + \frac{(\hbar k)^2 t}{2m\hbar} = \frac{kgt^2}{2} + \omega_{rec} t \ . \tag{4.5}$$

which is the phase difference of a particle wave function passing through a Ramsey-Bordé interferometer.

4.2.1.1 Bragg diffraction in a Ramsey-Bordé interferometer

Bragg diffraction couples two different momenta, namely, $|p\rangle$ and $|p + 2\hbar k_e\rangle$, in the Hilbert space of atomic motion which, as long as the atoms are not trapped, is considered continuous. As addressed elsewhere, the two coupled motional states can conveniently be regarded as a driven two-level system (76), so that Bragg diffraction can be interpreted as a Raman transition between them. The problem that arises when the atoms are additionally subject to external forces (*e.g.* mg) is they provide an additional coupling of two levels, since state $|p + 2\hbar k_e\rangle$ can also be reached from $|p\rangle$ simply by acceleration during a certain time, $|p + mgt\rangle$.

The problem is handled spanning a multi-dimensional Hilbert space, $H_{two-level} \otimes H_{motion}$, where discrete and continuous degrees of freedom are entangled, and propagating the wave function iteratively by concatenating the propagators of all experimental sequences,

$$|\psi_f\rangle = ... \times \exp\left(-\frac{\imath}{\hbar} \int_{t_j}^{t_{j+1}} \hat{H}_{j\rightarrow j+1}(t, k_j) dt\right) \times ... |\psi_0\rangle \ . \tag{4.6}$$

Hamiltonians $\hat{H}_{j\to j+1}(t,k_j)$ for all periods must be evaluated at different initial momenta $k_j = k(t_j)$ and are time-dependent because the atomic momenta increase over time due to gravitational acceleration. They are simply the solution of equation of motion $\hbar\dot{k}_z = mg$ with initial conditions $z(0) = z$ and $k_z(0) = k_z$, respectively, $k_z(0) = k_z + 2q$ where $q = \hbar k_e$,

$$\tilde{k}_z(t) = k_z + \frac{mg}{\hbar}t \qquad \text{and} \qquad \tilde{k}'_z(t) = k_z + 2q + \frac{mg}{\hbar}t\ . \tag{4.7}$$

the propagators then become

$$\begin{aligned}\exp\left(-\frac{\imath}{\hbar}\int_{t_j}^{t_{j+1}}\hat{H}_{j\to j+1}(t,k_j)dt\right) &= \exp\left[-\frac{\imath}{\hbar}\int_{t_j}^{t_{j+1}}\begin{pmatrix}\frac{\hbar^2}{2m}k_j(t) & \frac{\hbar}{2}\Omega_R(t_j)\\ \frac{\hbar}{2}\Omega_R(t_j) & \frac{\hbar^2}{2m}k_j(t)\end{pmatrix}dt\right]\\ &= \exp\left[-\frac{\imath}{\hbar}\begin{pmatrix}\frac{\hbar^2}{2m}\int_{t_j}^{t_{j+1}}\left(k_j+\frac{mg}{\hbar}t\right)^2dt & \frac{\hbar}{2}\Omega_R(t_{j+1}-t_j)\\ \frac{\hbar}{2}\Omega_R(t_{j+1}-t_j) & \frac{\hbar^2}{2m}\int_{t_j}^{t_{j+1}}\left(k_j+2q+\frac{mg}{\hbar}t\right)^2dt+\imath\delta\end{pmatrix}\right]\ .\end{aligned} \tag{4.8}$$

Due to that ansatz, internal excitation is treated as 'quantum' and motion is treated as 'classical'. Internal excitation occurs by a Raman transition, absorbing a quantized amount of momenta, whereas motion occurs classically, since gravity will act on the atoms continuously transferring momenta to them. As shown in Equation 4.8, there is a continuous way to obtain momenta ($\propto mg$) and a quantized type ($2q$). δ is the effective detuning between the two excitation states, *i.e.* $\Delta = 2\hbar q^2/m - \delta$ is the detuning of Bragg lasers from the recoil shift.

Substituting $\tilde{t} \equiv t - t_j$ and defining $k_{j+1} \equiv k_j + \frac{mg}{\hbar}t_j$ and $k'_j \equiv k_j + 2q$, the propagator is rewritten as

$$\exp\begin{pmatrix}-\imath\frac{\hbar}{2m}\int_0^\tau\left(k_{j+1}+\frac{mg}{\hbar}\tilde{t}\right)^2d\tilde{t} & -\imath\frac{1}{2}\Omega_R\tau\\ -\imath\frac{1}{2}\Omega_R\tau & -\imath\frac{\hbar}{2m}\int_0^\tau\left(k'_{j+1}+\frac{mg}{\hbar}\tilde{t}\right)^2d\tilde{t}+\imath\delta\end{pmatrix}\ . \tag{4.9}$$

Solving the integrals in the Hamiltonian leads to

$$\exp\left[-\imath\begin{pmatrix}\left(\frac{\hbar k_{j+1}^2}{2m}\tau+\frac{k_{j+1}g}{2}\tau^2+\frac{mg^2}{6\hbar}\tau^3\right) & \frac{\Omega_R}{2}\tau\\ \frac{\Omega_R}{2}\tau & \frac{1}{2}\left(\frac{\hbar k'^2_{j+1}}{2m}\tau+\frac{k'_{j+1}g}{2}\tau^2+\frac{mg^2}{6\hbar}\tau^3\right)+\imath\delta\tau\end{pmatrix}\right]\ . \tag{4.10}$$

As addressed elsewhere, a Ramsey-Bordé interferometer consists of a $\frac{\pi}{2}$-π-$\frac{\pi}{2}$ laser pulse sequence of Bragg diffraction pulses leading to splitting and recombination of an atomic wave-function in momentum space. Therefore, 5 sequences were chosen with the following settings:

$j \to j+1$	$\tau = t_{j+1} - t_j$	k_0 is the initial Gaussian thermal distribution
$0 \to 1$	$\frac{\pi}{2\Omega_R}$	$k_1 \simeq k_0 + \frac{mg}{\hbar}\frac{\pi}{2\Omega_R} \simeq k_0$
$1 \to 2$	τ	$k_2 = k_1 + \frac{mg}{\hbar}\tau$
$2 \to 3$	$\frac{\pi}{\Omega_R}$	$k_3 = k_2 + \frac{mg}{\hbar}\frac{\pi}{\Omega_R} \simeq k_2$
$3 \to 4$	τ	$k_4 = k_3 + \frac{mg}{\hbar}\tau$
$4 \to 5$	$\frac{\pi}{2\Omega_R}$	$k_5 = k_4 + \frac{mg}{\hbar}\frac{\pi}{2\Omega_R} \simeq k_4$

(4.11)

If the pulse duration is short, gravitational acceleration may be neglected during those pulses, recalling a change in the pulse duration will imply a change in Rabi frequency for the same type of pulse (π or $\pi/2$).

Substituting the final Equation 4.10 with the definitions in Equation 4.11 into Equation 4.6 leads to a formula that calculates Ramsey fringes,

$$NB(k_z)\langle\psi_{k_z,k_z+2q}(k_z)|\psi_f(k_z)\rangle \ , \tag{4.12}$$

where N is the total number of atoms and $B(k_z)$ is the Maxwell-Boltzmann distribution of initial atomic velocities,

$$B(k_z) = \sqrt{\frac{\hbar^2}{2\pi mk_BT}}e^{-\hbar^2k_z^2/(2mk_BT)} \ , \tag{4.13}$$

$i.e.$, populations $|\langle\psi_{k_z,k_z+2q}|\psi_f\rangle|^2$ are evaluated on a grid of momenta chosen in the $\hbar k_0 \in [-9,5]\sqrt{mk_BT}$ interval and then weighted with Maxwell-Boltzmann distribution.

Some results from the procedure are provided and discussed in what follows. Figure 27 showed momentum distributions of the atomic cloud directly after the first $\frac{\pi}{2}$-pulse, after π-pulse, and after the second $\frac{\pi}{2}$-pulse. The first $\frac{\pi}{2}$-pulse converts the initial Maxwell-Boltzmann distribution of the cold atomic cloud [blue line in Figure 27(a)] into a coherent superposition of two distributions separated by recoil momentum $2q$. π-pulse interchanges the momentum state populations and the second $\frac{\pi}{2}$-pulse mixes them, thus forming the Ramsey fringes. The modulations appearing in the curves of Figure 27(b) are due to the finite duration of the pulses (chosen as $T_R = 2\ \mu s$ in all simulations). Longer duration leads to much stronger distortions of the distributions.

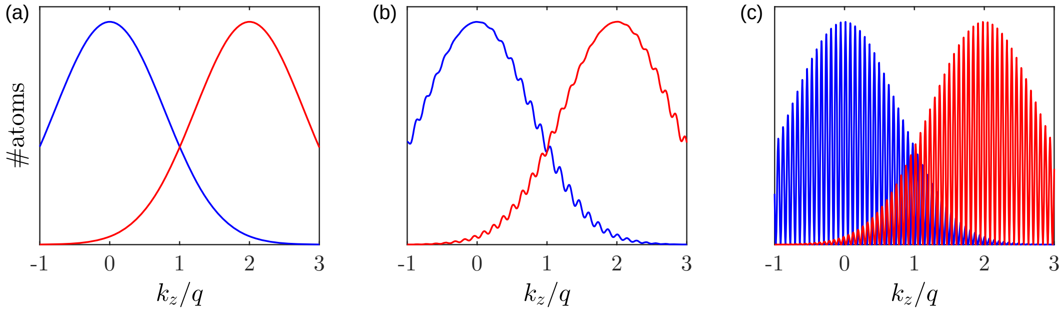

Figure 27 – Momentum distributions during a Ramsey-Bordé pulse sequence with $N = 10^5$ strontium atoms of temperature $T = 1\ \mu K$ subject to Bragg pulses at $\lambda_{brg} = 689\ nm$ ($^1S_0 \rightarrow {}^3P_1$) under 180° angle (a) after the first $\frac{\pi}{2}$-pulse, (b) after π-pulse, and (c) after the second $\frac{\pi}{2}$-pulse. The gravitational acceleration is $g = 9.81\ m/s^2$. Rabi frequency is $\Omega_R = (2\pi)\ 500\ kHz$ and free evolution time $\tau = 100\ \mu s$.

Source: By the author.

The advantage of the method is the program can be run faster with Equation 4.12, resulting in a process expedited by first identifying the state of the atom ($\langle\psi_{a,b}(k_z)|\psi_f(k_z)\rangle$)

and then incorporating the velocity distribution for the atoms, represented by $B(k_z)$. The approach yields the result for a single atom; however, the behaviour of many atoms is required. Instead of executing the program N times, it can be simply multiplied by N, since each iteration will lead to a specific point within $B(k_z)$ distribution. The results are then presented in terms of number of atoms in each momentum state, as shown in Figure 27.

The impact of finite temperature on the fringes was studied by Figure 28. The temperature of the atomic cloud was set to $T = 0.1\ \mu K$ in Figure 28(a,b) and to $T = 1\ \mu K$ in Figure 28(c,d). The width of the momentum distributions increases with temperature. Blue and cyan curves, taken at different gravitational accelerations g and $g(1 + 10^{-2})$, are clearly shifted, which points to a resolution limited at $\Delta g/g \approx 10^{-2}$ for those parameters, *i.e.*, a difference between the curves is observed only if our difference in gravity is above 10^{-2} m/s^2. However, whereas the contrast of the fringes diminishes with increasing temperature (because the atoms are distributed over more momenta), the shift, hence, the resolution, do not depend on temperature.

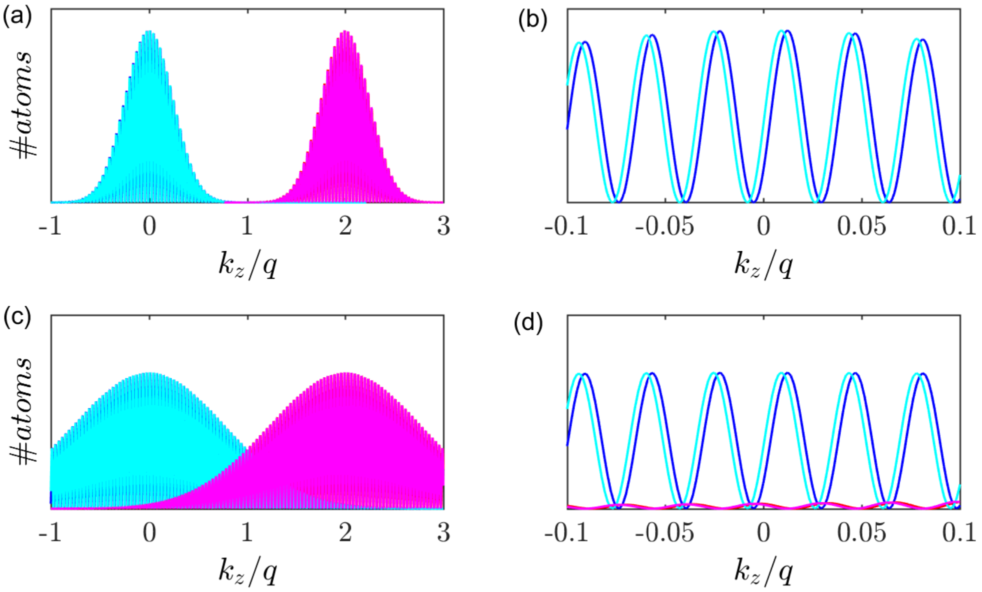

Figure 28 – Impact of temperature on Ramsey fringes. (a,b) $T = 0.1\ \mu K$ and (c,d) $T = 1\ \mu K$. Blue and red curves are calculated for $g = 9.81\ m/s^2$ and are below cyan and magenta. Cyan and magenta lines for $g(1 + 10^{-2})$. The other parameters are the same adopted in Figure 27, except for $\tau = 200\ \mu s$. (b,d) show the same image of (a,c), respectively, but a zoom near $k_z = 0$ enables distinguishing the blue curve from the cyan one, which represents a 10^{-2} difference in gravity. Since red and magenta curves are in a $B(k_z + 2q)$velocity distribution, they cannot be visualized in a zoomed image near $k_z = 0$.

Source: By the author.

According to Equation 4.5, the phase shift scales quadratically with free evolution time τ. Therefore, a resolution approaching 10^{-8} may be expected increasing the evolution time by three orders of magnitude to $\tau = 200\ ms$, as implemented in the first gravimeter experiments (75). Figure 29 showed Ramsey fringes calculated for three different free evolution times τ.

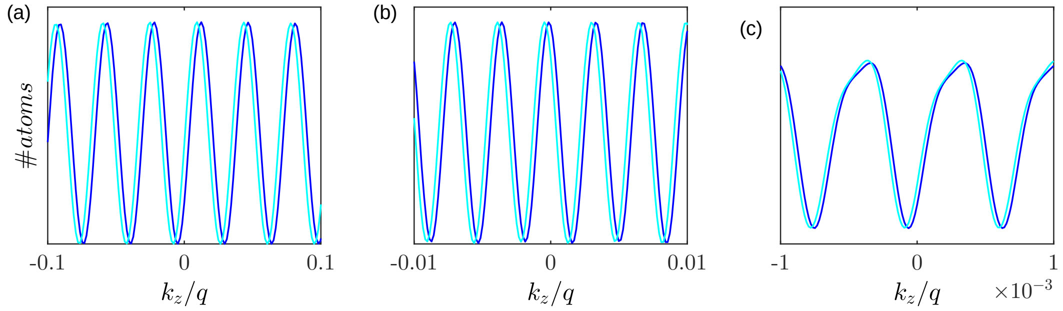

Figure 29 – Impact of the free evolution time duration on Ramsey fringes. Blue curves are calculated with $g = 9.81\ m/s^2$ and cyan ones are calculated with (a) $g = g(1+10^{-2})g$, $\tau = 200\ \mu s$, (b) $g = g(1+10^{-4})g$, $\tau = 2\ ms$, (c) $g = g(1+10^{-6})g$, $\tau = 20\ ms$. The other parameters are the same adopted in Figure 28. The images are zoomed in Figure 28(b,d) so that the difference between the curves can be visualized. For longer temporal evolution, the velocity distribution must be zoomed for the visualization of the difference in the signals.

Source: By the author.

Figure 29(c) shows the appearing of a plateau, which can be explained by a higher influence of Doppler effects due to longer temporal evolution τ. Therefore, the atoms can interact more with gravity, changing their velocities to higher ones, and the second $\pi/2-$pulse cannot bring the atoms to the necessary external state, *i. e.*, the momentum state.

4.2.2 Measured signals

If the atomic cloud is not much hotter than the single-photon recoil limit, *i.e.*,

$$\frac{k_B T}{2} < \frac{q^2}{2m} \equiv \hbar\omega_{rec}\ , \tag{4.14}$$

the fraction of atoms occupying both states $|p\rangle$ and $|p+2q\rangle$ is well separated in momentum space and can be evaluated separately via time-of-flight absorption imaging. (Note the momentum states are concomitant in different internal excitation states in many Ramsey-Bordé interferometers (75), facilitating their selective probing.) The measured quantities are, therefore,

$$\int_{-\infty}^{\infty} NB(k_z)\,|\langle p|\psi_f(k_z)\rangle|^2\,dk_z \qquad \text{and} \qquad \int_{-\infty}^{\infty} NB(k_z)\,|\langle p+2q|\psi_f(k_z)\rangle|^2\,dk_z\ , \tag{4.15}$$

i.e., the number of atoms is quantified in each state $|p\rangle$ and $|p+2q\rangle$, taking into account the Maxwell-Boltzmann distribution of velocities. The measurement is performed for each value of gravity within the $(9.810, 9.815)\ m/s^2$ interval. According to Equation 4.15, the experimentally observed signal corresponds to a sum over different velocity classes of atoms, *i.e.*, in agreement with Equation 4.13. Figure 30 provided a plot of such a signal.

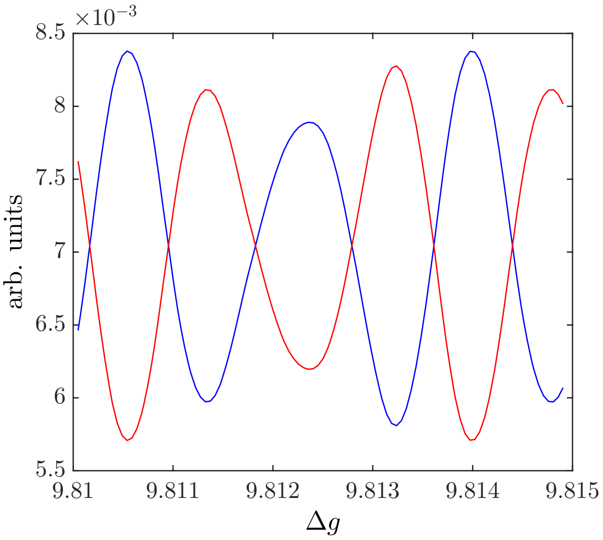

Figure 30 – Number of atoms that can be attributed to one of the momenta states $|p\rangle$ (blue curve) or $|p+2q\rangle$ (red curve) as a function of gravity. Here, $T = 1\ \mu K$, $\tau = 10\ ms$, $\Omega_R = (2/\pi)\ 1\ MHz$.

Source: By the author.

5 CONCLUSIONS

This dissertation has summarized our recent efforts for setting up an experiment that demonstrates a matter-wave interferometry based on the interaction of ultracold strontium atoms via a narrow dipole-forbidden transition with the light modes supported by an optical ring cavity operated in the 'bad cavity' limit.

The main goal of the experiment, which is the non-destructive monitoring of Bloch oscillations performed by the atoms in the field of gravity due to their interaction with the cavity fields, has not yet been reached. However, a big step has been taken with the observation of effects, not only proving the presence of strong collective coupling between atoms and light fields, but also indicating the possible existence of non-classical interatomic correlations in certain parameter regimes. Indeed, the normal mode splitting of the cavity transmission spectra, expected for strong collective coupling, exhibits an additional hitherto unobserved feature when both laser and cavity mode frequency are tuned to resonance with atomic transition. In this spectral regime, the coupled atom-cavity system exhibits a bistable behaviour, detected in our measurements and associated with the fact our system was strongly saturated. We argued bi-stability must be due to non-linear features in the Hamiltonian of the coupled system and pointed out such non-linearities are expected to generate non-classical interatomic correlations in the bad-cavity limit.

Towards preparing the ground for future measurements implementing a Ramsey-Bordé-type matter-wave interferometer, the atomic momentum distribution was simulated applying a $\pi/2$-π-$\pi/2$-spin echo-type pulse sequence. Using 1 μK cold strontium atoms driven on ${}^1S_0 \rightarrow {}^3P_1$ transition (689 nm), a precision in the determination of gravitational acceleration of $\Delta g/g < 10^{-8}$ could be reached with $\pi/2$ pulse durations not exceeding $T_R = 2\ \mu s$ and free evolution times longer than $\tau = 200\ ms$.

Future studies can (i) exploit the saturation-induced non-linearity in quantum noise suppressing protocols, such as spin-squeezing or super-radiant lasing, (ii) search for signatures of Bloch oscillations with an improved (*i.e.* mechanically more stable) experimental setup, and (iii) implement Ramsey-Bordé-type pulse sequences for an alternative measurement of gravitational forces.

REFERENCES

1 ARANTES, J. T. **Especialistas debatem as tecnologias quânticas emergentes e os estudos em andamento no Brasil**. 2021. Available at: https://agencia.fapesp.br/especialistas-debatem-as-tecnologias-quanticas-emergentes-e-os-estudos-em-andamento-no-brasil/35810. Accessible at: 18 Oct. 2023.

2 PACETE, L. G. **Computação quântica será realidade no Brasil em 2025, diz CEO DA IBM**. 2022. Available at: https://forbes.com.br/forbes-tech/2022/11/computacao-quantica-sera-realidade-no-brasil-em-2025-diz-ceo-da-ibm/. Accessible at: 18 Oct. 2023.

3 REDE NACIONAL DE ENSINO E PESQUISA. **Os desafios das tecnologias quânticas no Brasil e no mundo é tema central de evento**. 2021. Available at: https://www.rnp.br/noticias/os-desafios-das-tecnologias-quanticas-no-brasil-e-no-mundo-e-tema-central-de-evento. Accessible at: 18 Oct. 2023.

4 BRASIL. Ministério da Ciência, Tecnologia e Inovação. **MCTI busca fortalecer parcerias em computação e tecnologias quânticas entre Brasil e Rússia**. 2023. Available at: https://www.gov.br/mcti/pt-br/acompanhe-o-mcti/noticias/2023/08/mcti-busca-fortalecer-parcerias-em-computacao-e-tecnologias-quanticas-entre-brasil-e-russia. Accessible at: 18 Oct. 2023.

5 EMBRAPII. **Levantamento internacional aponta Embrapii como única iniciativa latina em tecnologia quântica**. 2023. Available at: https://embrapii.org.br/levantamento-aponta-embrapii-unica-iniciativa-america-latina-tecnologia-quantica/. Accessible at: 18 Oct. 2023.

6 MOREIRA, A. C. **A tecnologia quântica de segunda geração vai chegar ao Brasil?** 2023. Available at: https://jornal.unesp.br/2023/02/06/a-tecnologia-quantica-de-segunda-geracao-vai-chegar-ao-brasil/. Accessible at: 18 Oct. 2023.

7 FRAGALLE, E. **Especialistas dizem que Brasil deve ser o centro da ciência quântica aplicada ao agro**. 2023. Available at: https://www.embrapa.br/busca-de-noticias/-/noticia/79350113/especialistas-dizem-que-brasil-deve-ser-o-centro-da-ciencia-quantica-aplicada-ao-agro. Accessible at: 18 Oct. 2023.

8 MOOR INSIGHTS AND STRATEGY. **Quantum USA vs. quantum China**: the world's most important technology race. 2019. Available at: https://www.forbes.com/sites/moorinsights/2019/10/10/quantum-usa-vs-quantum-china-the-worlds-most-important-technology-race/?sh=7e80ead672de. Accessible at: 18 Oct. 2023.

9 SWAYNE, M. **Top quantum spenders based on GDP**: list offers surprising changes in leadership status. 2023. Available at: https://thequantuminsider.com/2023/02/28/top-quantum-spenders-based-on-gdp-list-offers-surprising-changes-in-leadership-status/. Accessible at: 18 Oct. 2023.

10 BOLADIAN, R. *et al.* **The rise of national quantum strategies**. 2023. Available at: https://www.kearney.com/industry/aerospace-defense/article/-/insights/the-rise-of-national-quantum-strategies. Accessible at: 18 Oct. 2023.

11 GOVERNMENT OF CANADA. **Canada's national quantum strategy**. 2023. Available at: https://ised-isde.canada.ca/site/national-quantum-strategy/en/canadas-national-quantum-strategy. Accessible at: 18 Oct. 2023.

12 INDIA. Ministry of Science & Technology. **Budget 2020 announces the largest ever science mission**. 2020. Available at: https://pib.gov.in/PressReleseDetailm.aspx?PRID=1601563. Accessible at: 18 Oct. 2023.

13 VIEIRA, C. *et al.* Exploring quantum thermodynamics with nmr. **Journal of Magnetic Resonance Open**, v. 16–17, p. 100105, Mar. 2023. DOI: 10.1016/j.jmro.2023.100105.

14 OLIVEIRA, M. H. *et al.* Steady-state entanglement generation for nondegenerate qubits. **Physical Review A**, v. 107, n. 2, p. 023706, 2023. DOI: 10.1103/physreva.107.023706.

15 ROUXINOL, F. *et al.* Measurements of nanoresonator-qubit interactions in a hybrid quantum electromechanical system. **Nanotechnology**, v. 27, n. 36, p. 364003, Aug. 2016. DOI: 10.1088/0957-4484/27/36/364003.

16 CHERUBIM, C.; BRITO, F.; DEFFNER, S. Non-thermal quantum engine in transmon qubits. **Entropy**, v. 21, n. 6, 2019. DOI: 10.3390/e21060545.

17 RIBEIRO, B. A. *et al.* Exploring entanglement in open cavity parametric oscillators: From triply to doubly resonant cavities. **Physical Review A**, v. 102, n. 2, p. 023522, Aug. 2020. DOI: 10.1103/physreva.102.023522.

18 CARVALHO, N. C. *et al.* High-frequency gaas bullseye optomechanical resonator. *In*: CONFERENCE ON LASERS AND ELECTRO-OPTICS. San Jose. **Proceedings** [...] San Jose: IEEE, 2020.

19 GUERRERO, A. M. *et al.* Continuous variable entanglement in an optical parametric oscillator based on a nondegenerate four wave mixing process in hot alkali atoms. **Physical Review Letters**, v. 129, p. 163601, Oct. 2022. DOI: 10.1103/PhysRevLett.129.163601.

20 UNIVERSIDADE DE SÃO PAULO. Philippe Wilhelm Courteille; Pierre Marcel Bachelard Romain. **Device and method for gravitational acceleration measurement**. BR 102015007944-3 A2, 09 April 2015, 07 Nov. 2017.

21 CHEN, Z. *et al.* Enhancing strontium clock atom interferometry using quantum optimal control. **Physical Review A**, v. 107, p. 063302, June 2023. DOI: 10.1103/PhysRevA.107.063302.

22 DEGEN, C. L.; REINHARD, F.; CAPPELLARO, P. Quantum sensing. **Reviews of Modern Physics**, v. 89, p. 035002, July 2017. DOI: 10.1103/RevModPhys.89.035002.

23 BASS, S. D.; DOSER, M. **Quantum sensing for particle physics**. 2023. Available at: https://cds.cern.ch/record/2866747/files/2305.11518.pdf. Accessible at: 22 Dec. 2023.

24 LANZAGORTA, M.; UHLMANN, J.; VENEGAS-ANDRACA, S. E. Quantum sensing in the maritime environment. *In*: OCEANS 2015 - MTS/IEEE. 2015, Washington. **Proceedings** [...] Washington: IEEE, 2015. p. 1–9.

25 GEFEN, T.; ROTEM, A.; RETZKER, A. Overcoming resolution limits with quantum sensing. **Nature Communications**, v. 10, n. 1, p. 4992, Nov. 2019. DOI: 10.1038/s41467-019-12817-y.

26 RODRÍGUEZ, D. A quantum sensor for high-performance mass spectrometry. **Applied Physics B**, v. 107, n. 4, p. 1031–1042, June 2012. DOI: 10.1007/s00340-011-4824-5.

27 HELLAND, A. **Observations of gravity field variations from ground and satellite data**. 2013. Dissertation (Master) — Norwegian University of Life Sciences, Ås, 2013.

28 TÓTH, G. Y.; VÖLGYESI, L. Local gravity field modeling using surface gravity gradient measurements. *In*: TREGONING, P.; RIZOS, C. (ed.). **Dynamic Planet:** monitoring and understanding a dynamic planet with geodetic and oceanographic tools IAG symposium Cairns, Australia 22–26 August, 2005. Berlin, Heidelberg: Springer, 2007. p. 424–429.

29 ETEJE, S. O.; ODUYEBO, O. F.; OLUYORI, P. D. Modelling local gravity anomalies from processed observed gravity measurements for geodetic applications. **International Journal of Scientific Research in Science and Technology**, v. 6, n. 5, p. 144–162, 2019. DOI: 10.32628/IJSRST196515.

30 BORDÉ, C. J. *et al.* Optical ramsey fringes with traveling waves. **Physical Review A**, v. 30, p. 1836–1848, Oct. 1984. DOI: 10.1103/PhysRevA.30.1836.

31 OLSON, J. *et al.* Ramsey-bordé matter-wave interferometry for laser frequency stabilization at 10^{-16} frequency instability and below. **Physical Review Letters**, v. 123, p. 073202, Aug. 2019. DOI: 10.1103/PhysRevLett.123.073202.

32 MORGENWEG, J.; BARMES, I.; EIKEMA, K. S. E. Ramsey-comb spectroscopy with intense ultrashort laser pulses. **Nature Physics**, v. 10, n. 1, p. 30–33, Jan. 2014. DOI: 10.1038/nphys2807.

33 MCALPINE, K. E.; GOCHNAUER, D.; GUPTA, S. Excited-band bloch oscillations for precision atom interferometry. **Physical Review A**, v. 101, p. 023614, Feb. 2020. DOI: 10.1103/PhysRevA.101.023614.

34 CLADÉ, P. Bloch oscillations in atom interferometry. **Rivista del Nuovo Cimento**, v. 38, n. 4, p. 173–207, Apr. 2015. DOI: 10.1393/ncr/i2015-10111-3.

35 KRAMIDA, A. *et al.* **NIST atomic spectra database (ver. 5.10)**. 2022. Available at: https://physics.nist.gov/asd. Accessible at: 9 Nov. 2023.

36 POLI, N. **Raffreddamento ed intrappolamento di atomi di stronzio**: verso un nuovo standard di frequenza nella regione ottica. 2005. 167 p. Thesis (Dottorato in Fisica) — Universit'a degli Studi di Firenze, Florence, 2005.

37 MICKELSON, P. G. *et al.* Spectroscopic determination of the s-wave scattering lengths of 86Sr and 88Sr. **Physical Review Letters**, v. 95, n. 22, p. 223002–223002, 2005. DOI: 10.1103/PHYSREVLETT.95.223002.

38 YAMAGUCHI, A. *et al.* A strontium optical lattice clock. **Journal of the National Institute of Information and Communications Technology**, v. 57, n. 3/4, p. 145, 2010.

39 NORCIA, M. A. *et al.* Superradiance on the millihertz linewidth strontium clock transition. **Science Advances**, v. 2, n. 10, p. e1601231, 2016. DOI: 10.1126/sciadv.1601231.

40 HOBSON, R. *et al.* Cavity-enhanced non-destructive detection of atoms for an optical lattice clock. **Optics Express**, v. 27, n. 26, p. 37099–37110, Dec. 2019. DOI: 10.1364/OE.27.037099.

41 THOMSEN, J. W. *et al.* Strontium optical lattice clock with high accuracy and stability. *In*: CONFERENCE ON PRECISION ELECTROMAGNETIC MEASUREMENTS DIGEST. 2008, Broomfield. **Proceedings** [...] Broomfield: IEEE, 2008. p. 90–91.

42 CHEN, C.-C. *et al.* Continuous guided strontium beam with high phase-space density. **Physical Review Applied**, v. 12, p. 044014, Oct. 2019. DOI: 10.1103/PhysRevApplied.12.044014.

43 SORRENTINO, F. *et al.* Laser cooling and trapping of atomic strontium for ultracold atoms physics, high-precision spectroscopy and quantum sensors. **Modern Physics Letters B**, v. 20, n. 21, p. 1287–1320, 2006. DOI: 10.1142/S0217984906011682.

44 MAZZONI, T. *et al.* Large-momentum-transfer bragg interferometer with strontium atoms. **Physical Review A**, v. 92, p. 053619, Nov. 2015. DOI: 10.1103/PhysRevA.92.053619.

45 RUDOLPH, J. *et al.* Large momentum transfer clock atom interferometry on the 689 nm intercombination line of strontium. **Physical Review Letters**, v. 124, p. 083604, Feb. 2020. DOI: 10.1103/PhysRevLett.124.083604.

46 YE, J.; LYNN, T. W. Applications of optical cavities in modern atomic, molecular, and optical physics. *In*: BEDERSON, B.; WALTHER, H. (ed.). **Advances in atomic, molecular, and optical physics**. Amsterdam: Elsevier, 2003. (Advances in atomic, molecular, and optical physics, v. 49), p. 1–83.

47 SLAMA, S. *et al.* Superradiant rayleigh scattering and collective atomic recoil lasing in a ring cavity. **Physics Review Letters**, v. 98, p. 053603, Feb. 2007. DOI: 10.1103/PhysRevLett.98.053603.

48 BUX, S. *et al.* Cavity-controlled collective scattering at the recoil limit. **Physical Review Letters**, v. 106, n. 20, 2011. DOI: 10.1103/physrevlett.106.203601.

49 SAMOYLOVA, M. *et al.* Mode-locked bloch oscillations in a ring cavity. **Laser Physics Letters**, v. 11, n. 12, p. 126005, Nov. 2014. DOI: 10.1088/1612-2011/11/12/126005.

50 SAMOYLOVA, M. *et al.* Synchronization of bloch oscillations by a ring cavity. **Optics Express**, v. 23, n. 11, p. 14823–14835, June 2015. DOI: 10.1364/OE.23.014823.

51 HODGSON, N.; WEBER, H. The fabry perot resonator. *In*: HODGSON, N.; WEBER, H. (ed.). **Optical resonators:** fundamentals, advanced concepts and applications. London: Springer, 1997. p. 137–162.

52 SANTOS, G. H. *et al.* Decomposing spatial mode superpositions with a triangular optical cavity. **Physical Review Applied**, v. 16, p. 034008, Sept. 2021. DOI: 10.1103/PhysRevApplied.16.034008.

53 RIVERO, D. **Observation of collective bistability in an ultracold cloud of strongly driven strontium atoms interacting with a ring cavity**. 2022. Thesis (Doctor in Science) — Instituto de Física de São Carlos, Universidade de São Paulo, São Carlos, 2022.

54 RIVERO, D. *et al.* Quantum resonant optical bistability with a narrow atomic transition: Bistability phase diagram in the bad cavity regime. **New Journal of Physics**, v. 25, n. 9, p. 093053, 2023. DOI: 10.1088/1367-2630/acf954.

55 SHANKAR, R. **Principles of quantum mechanics**. 2nd ed. New York: Springer, 2014.

56 GRIFFITHS, D. J.; SCHROETER, D. F. **Introduction to quantum mechanics**. 3rd ed. Cambridge: Cambridge University Press, 2020.

57 COURTEILLE, P. W. **Quantum mechanics applied to atoms and light**. São Carlos: IFSC, 2023. Available at: https://www.ifsc.usp.br/~strontium/. Accessible at: 22 Dec. 2023.

58 SAKURAI, J. J.; NAPOLITANO, J. **Mecânica quântica moderna**. 2nd ed. Cambridge: Cambridge University Press, 2021.

59 WALLS, D. F.; MILBURN, G. J. **Quantum optics**. Berlin, Heidelberg: Springer-Verlag, 1994.

60 SCULLY, M. O.; ZUBAIRY, M. S. **Quantum optics**. Cambridge: Cambrigde University Press, 1997.

61 GRIFFITHS, D. J. **Introduction to electrodynamics**. 4th ed. Cambridge: Cambridge University Press, 2013.

62 BERMAN, P. R. **Atom interferometry**. San Diego: Academic Press, 1997.

63 FOOT, C. J. The interaction of atoms with radiation. *In*: FOOT, C. J. (ed.). **Atomic physics**. Oxford: Oxford University Press, 2007. p. 123–125.

64 CHIH, L.-Y.; HOLLAND, M. Reinforcement-learning-based matter-wave interferometer in a shaken optical lattice. **Physical Review Research**, v. 3, p. 033279, Sept. 2021. DOI: 10.1103/PhysRevResearch.3.033279.

65 ASHCROFT, N. W.; MERMIN, N. D. **Solid state physics**. Fort Worth, Philadelphia: Saunders College, 1988.

66 CALLAWAY, J. **Quantum theory of the solid state**. New York: Academic Press, 1974.

67 JONES, W.; MARCH, N. H. **Theoretical solid state physics**. New York: Dover, 1985.

68 KITTEL, C. **Introdução à física do estado sólido**. Rio de Janeiro, RJ: LTC, 2006.

69 SILVA, C. B. **Development of a stable diode laser system for cavity-assisted matter-wave interferometry**. June 2020. Dissertation (Master in Science) — Departamento de Física, Universidade Federal de São Carlos, São Carlos, 2020.

70 ARMIJOS, M. A. M. **Construction of an experiment providing cold strontium atoms for atomic interferometry in a ring cavity**. June 2020. Dissertation (Master in Science) — Instituto de Física de São Carlos, Universidade de São Paulo, São Carlos, 2020.

71 RIVERO, D. *et al.* High-resolution laser spectrometer for matter wave interferometric inertial sensing with non-destructive monitoring of bloch oscillations. **Applied Physics B**, v. 128, n. 3, p. 44, Feb. 2022. DOI: 10.1007/s00340-022-07772-4.

72 PHILLIPS, W. D.; METCALF, H. Laser deceleration of an atomic beam. **Physical Review Letters**, v. 48, p. 596–599, Mar. 1982. DOI: 10.1103/PhysRevLett.48.596.

73 ALI, D. B. *et al.* Detailed study of a transverse field zeeman slower. **Journal of Physics B: Atomic, Molecular and Optical Physics**, v. 50, n. 5, p. 055008, Feb. 2017. DOI: 10.1088/1361-6455/aa5a6a.

74 HOROWITZ, P.; HILL, W. Phase-locked loops. *In*: HOROWITZ, P.; HILL, W. (ed.). **The art of electronics**. New York: Cambridge University Press, 2016. p. 955–974.

75 KASEVICH, M.; CHU, S. Atomic interferometry using stimulated raman transitions. **Physics Review Letters**, v. 67, p. 181–184, July 1991. DOI: 10.1103/PhysRevLett.67.181.

76 KOZUMA, M. *et al.* Coherent splitting of bose-einstein condensed atoms with optically induced bragg diffraction. **Physical Review Letters**, v. 82, p. 871–875, Feb. 1999. DOI: 10.1103/PhysRevLett.82.871.

APPENDIX

APPENDIX A – SCHRÖDINGER EQUATION SOLUTION

Beginning with Equation 2.3, where $\hat{H}_0 = \frac{E_a+E_b}{2}\hat{\sigma}_0 + \frac{\hbar\omega_0}{2}\hat{\sigma}_z$, it can be rewritten in a matrix form with $\hbar\omega_0 = E_b - E_a$, as

$$\hat{H}_0 = \begin{bmatrix} E_b & 0 \\ 0 & E_a \end{bmatrix}$$

a transformation to a frame rotating is performed at frequency ω, such that

$$\vec{\psi}(\vec{r},t) = e^{i(\omega t+\varphi)\frac{\hat{\sigma}_z}{2}}\vec{\Psi}(\vec{r},t). \tag{A.1}$$

Applying the transformation from Equation A.1 to Equation 2.3 leads to the new Schrödinger equation

$$i\hbar\frac{\partial}{\partial t}\vec{\psi}(\vec{r},t) = \left[-\frac{\hbar\omega}{2}\hat{\sigma}_z - \frac{\hbar^2}{2M}\vec{\nabla}^2 + \hat{H}_0 + \hat{H}_1^{'}\right]\vec{\psi}(\vec{r},t), \tag{A.2}$$

where $\hat{H}_1^{'}$ is given according to the elements of the electric dipole Hamiltonian matrix and, after using Equation A.1, becomes

$$\hat{H}_1^{'} = \begin{bmatrix} V_{bb} & -\hbar\Omega e^{i\vec{K}\cdot\vec{r}} \\ -\hbar\Omega e^{-i\vec{K}\cdot\vec{r}} & V_{aa} \end{bmatrix}.$$

A stationary solution for plane waves is now assumed and the variables are separated such that wave function $\vec{\psi}(\vec{r},t)$ is split into two parts, according to its momentum, and rewritten as

$$\vec{\psi}(\vec{r},t) = \begin{bmatrix} \vec{\psi}_{b,\vec{k}_e}(\vec{r},t) \\ \vec{\psi}_{a,0}(\vec{r},t) \end{bmatrix} = \begin{bmatrix} e^{i(\vec{K}+\vec{k}_e)\cdot\vec{r}} & 0 \\ 0 & e^{i\vec{K}\cdot\vec{r}} \end{bmatrix}\hat{\psi}(t), \tag{A.3}$$

where

$$\hat{\psi}(t) = \begin{bmatrix} u_{b,\vec{k}_e}(\vec{p}) \\ u_{a,0}(\vec{p}) \end{bmatrix} e^{-iEt/\hbar}. \tag{A.4}$$

Using Equation A.3 and Equation A.4 in Equation A.2leads to

$$i\hbar\frac{\partial}{\partial t}\hat{\psi}(t) = \left[\hat{H}_0 - \frac{\hbar\omega}{2}\hat{\sigma}_z + \left(\begin{bmatrix} \frac{\hbar^2}{2m}\left(\vec{K}+\vec{k}_e\right)^2 + V_{bb} & -\hbar\Omega \\ -\hbar\Omega & \frac{\hbar^2}{2m}\vec{K}^2 + V_{aa} \end{bmatrix}\right)\right]\hat{\psi}(t) = E\hat{\psi}(t) \tag{A.5}$$

whose solution results in

$$\begin{aligned} &\left[\frac{\hbar^2}{2M}\left(\vec{K}^2+\vec{k}^2\right) - \frac{p^2}{2M} + V_{bb} + \hbar(\omega_0-\omega_L)\right]u_{b,\vec{k}}(\vec{p}) - \hbar\Omega u_{a,0}(\vec{p}) = 0, \\ &-\hbar\Omega u_{b,\vec{k}}(\vec{p}) + \left[\frac{\hbar^2\vec{K}^2}{2M} - \frac{p^2}{2M} + V_{aa}\right]\hbar\Omega u_{a,0}(\vec{p}) = 0. \end{aligned} \tag{A.6}$$